3-D Simulation of Rapid Melting and Re-crystallization of Silicon Thin Films by Excimer Laser Using Cellular Automata Algorithm

Hidayat Kisdarjono
B.S., Institut Teknologi Bandung, 1993
M.S., Oregon Graduate Institute, 1995

A thesis presented to the faculty of the
OGI School of Science & Engineering
at Oregon Heath & Science University
in partial fulfillment of the
requirements for the degree
Doctor of Philosophy
in
Electrical and Computer Engineering

February, 2004

The dissertation "3-D Simulation of Rapid Melting and Re-crystallization of Silicon Thin Films by Excimer Laser Using Cellular Automata Algorithm" by Hidayat Kisdarjono has been examined and approved by the following Examination Committee:

Dr. Raj Solanki, Thesis Advisor
Professor

Dr. Apostolos T. Voutsas
Sharp Laboratories of America

Dr. John L. Freeouf
Professor

Dr. Shankar Rananavare
Research Associate Professor

ACKNOWLEDGEMENTS

First of all, I would like to thank Raj Solanki, my thesis advisor, for the support and guidance he has given me during my time at OGI. I am also grateful for his invaluable input during the writing of this dissertation.

My thanks also go to Tolis Voutsas, form Sharp Laboratories of America, for initiating the project and for providing the critical data in this dissertation. Working with Tolis has taught me a great deal about the art of doing research.

I would also like to thank two other professors at OGI and members of my thesis committee, Shankar Rananavare and John Freeouf, for their suggestions for revising the earlier versions of my dissertation.

To my parents who never fail to support me in everything I do, far away they may be, I would be forever indebted. And finally, for those closest to me – Fiona, Alia and Anika – I am grateful for their tremendous patience, generosity and love.

TABLE OF CONTENTS

LIST OF FIGURES

LIST OF TABLES

LIST OF SYMBOLS

A	multiplier
C	increment
c	speed of light in vacuum
c_p	specific heat
d	thickness
E	electric field
ED	energy density
$F(z)$	laser power density as a function of depth
f	fraction of molecule absorbed
$f(\theta)$	contact angle correction factor
$\dot{G}$	growth rate
H	magnetic field
$I_a(T)$	nucleation rate
I_{oa}	kinetic prefactor for heterogeneous nucleation
I_{ov}	kinetic prefactor for homogeneous nucleation
$I_t(t)$	laser relative intensity as a function of time
$I_x(x)$	laser relative intensity as a function of time
K	proportionality constant for the linearized interface response function
k	wave number

k_B	Boltzmann's constant
M	modulus
n	index of refraction
n_{liquid}	number of molecules in the liquid facing a unit area of interface
n_α	number of molecules in the solid facing a unit area of interface
n^*	complex index of refraction
$P_{liquid}(T, t)$	probability of a cell remaining liquid
R	reflectivity, ratio of the reflected to the incident energy for normal incedence
S_{Laser}	volumetric energy source for the absorbed laser energy
$S_{\Delta Hm}$	volumetric energy source for latent heat released/absorbed during phase change.
T	absolute temperature
t	time
T_{int}	temperature at the solid-liquid interface
T_m	equilibrium melting temperature
U	random fraction
v	velocity
v_{int}	interface velocity (normal)
V_{LC}	applied potential across liquid crystal
X	random integer
α	absorption coefficient

Γ	instantaneous nucleation frequency of a cell
ΔA	area of the base of a cell
ΔG_{ls}	free energy of formation
ΔG_t^*	activation energy for interface crossing
Δn	refractive index anisotropy
Δt	time step
ΔV	volume of a cell
ε	permittivity
θ	contact angle
θ_i	angle of incedence
θ_t	angle of transmission
θ_r	angle of reflection
κ	thermal conductivity
λ	wavelength
μ	permeability
ρ	density
σ	surface energy
τ	time
Φ	phase
ω	temporal frequency

LIST OF ACCRONYMS AND ABBREVIATIONS

a-Si	amorphous silicon
CA	cellular automata
CNT	classical nucleation theory
ELC	excimer laser crystallization
FEM	finite element method
IRF	interface response function
ITO	indium tin oxide
KrF	krypton fluoride
LCD	liquid crystal display
LGL	lateral growth length
MISPC	Metal-Induced Solid Phase Crystallization
n-MOS	n-type metal-oxide-semiconductor
PECVD	plasma enhanced chemical vapor deposition
p-MOS	n-type metal-oxide-semiconductor
poly-Si	polycrystalline silicon
SEM	scanning electron microscope
SiNx	silicon nitride
SiO_2	silicon dioxide
SLS	Sequential Lateral Solidification

SPC	solid phase crystallization
TFT	thin film transistor
TN	twisted nematic
UV	ultra violet
XeCl	xenon chloride

ABSTRACT

As flat panel displays shrink in size, thin film transistor (TFT) technology is driven to improve display resolution (i.e. reduce pixel transistor size) and to integrate more functionality (i.e. circuitries) onto the display substrate. Thus, a key TFT process is the fabrication of higher quality silicon active layer on the amorphous display substrate. Excimer-laser-annealing (ELA) is one method by which energy is delivered to melt amorphous silicon films to produce directionally solidified, high quality silicon crystals without causing extensive heating of the substrate.

Due to its technological importance, it is desirable to simulate this process in order to fully understand the mechanisms involved and to optimize the conditions leading to desirable microstructure. In this investigation, a model has been developed for the rapid melting and re-crystallization of thin silicon films induced by ELA. The central feature of this model is its ability to simulate lateral growth and random nucleation. The first component of the model is a set of rules for phase change. The second component is a set of functions for computing the latent heat and the displacement of the solid-liquid interface resulting from the phase change. The third component is an algorithm that allows for random nucleation based on classical nucleation theory (CNT). Consequently, the model enables the prediction of lateral growth length (LGL), as well as the calculation of other critical responses of the quenched film such as solid-liquid interface velocity and undercooling.

To validate the model, thin amorphous Si films with thickness of 30nm, 50nm and 100nm were annealed under various laser fluences to completely melt the films. The resulting LGL were measured using a scanning electron microscope (SEM). Using physical parameters that were consistent with previous studies, the simulated LGL values agree well with the experimental results over a wide range of irradiation conditions. Sensitivity analysis was done to demonstrate the behavior of the model with respect to a select number of model parameters. Our simulations suggest that, for a given fluence,

controlling the film's quenching rate is essential for increasing LGL. To this end, the model is an invaluable tool for evaluating and choosing irradiation strategies for increasing lateral growth in laser-crystallized silicon films.

CHAPTER 1: INTRODUCTION

In liquid crystal display (LCD) fabrication, the requirement for a substrate that is both transparent and inexpensive has made glass the material of choice. Thin film transistors (TFTs) produced on glass, however, are inferior to transistors produced on single crystalline silicon. In most practical cases, silicon film deposited over glass inherits the amorphous structure of glass and, therefore, incorporates higher level of defects than in single crystalline silicon. For this reason, TFTs with amorphous silicon (a-Si) active regions have one main disadvantage, namely, lower carrier mobility [1, 2]. Recently, to improve the performance of TFTs in LCDs, excimer lasers have been used to deliver high concentration of energy to completely melt the thin a-Si films. Under favorable conditions, subsequent re-crystallization can result in large-grained polysilicon (poly-Si) materials [3, 4, 5, 6, 7]. With higher carrier mobility, such material allows for faster and more efficient devices. The process, referred to as excimer laser crystallization (ELC), enables the fabrication of high quality silicon on glass instead of on the more heat resistant (but more costly) quartz.

ELC is a promising technique for producing poly-Si material for TFT fabrication. Therefore, it is desirable to simulate this process in order to fully understand the mechanisms involved and to optimize the conditions leading to desirable microstructure. With the exception of the work by Im and coworkers, previous laser crystallization models were developed based on the assumption that phase change is determined by temperature alone, i.e. thermodynamically driven [8, 9, 10, 11]. Unfortunately, such assumption precludes phenomena such as sharp solid-liquid interfaces, undercooling and random nucleation which are typically seen in ELC. Simulations based on such models

have not yield accurate picture of the ELC process. Therefore, this investigation was undertaken to develop a physically consistent model which takes into account the critical mechanisms in ELC so physically meaningful simulations can be performed. The results of this investigation are presented in this dissertation.

In this chapter, basic operations of TFT-LCD and the evolution of poly-Si technology leading up to ELC process are discussed. An overview of pertinent experimental results on nucleation and previous laser annealing models are also presented. Finally, this chapter introduces the key approach for properly treating the problems of phase transformation and random nucleation.

1.1 TFT

TFTs are field effect transistors fabricated into thin semiconductor films on insulating substrates. Such transistors are used on LCD panels, which are fabricated on glass or quartz. Unlike transistors built on single-crystal silicon, TFTs are made of amorphous or polycrystalline active layer. The basic structure of TFT (n-MOS) can be seen in fig. 1.1 An n-MOS TFT has a p-type region called channel between two n^+-type regions called source and drain. Conversely, a p-MOS TFT has an n-type channel between two p^+-type source and drain. Above the channel is the gate, comprising a thin layer of insulator (e.g., SiO_2) with poly-silicon layer above it. TFTs operate as field effect transistors. The channel is in effect a capacitor plate on which, by application of bias, minority carriers gather. In an n-MOS TFT, for example, a sufficiently large positive gate bias attracts electrons to the channel. These electrons make it possible for current to flow from source to drain, producing transfer characteristics shown in fig.1.2.

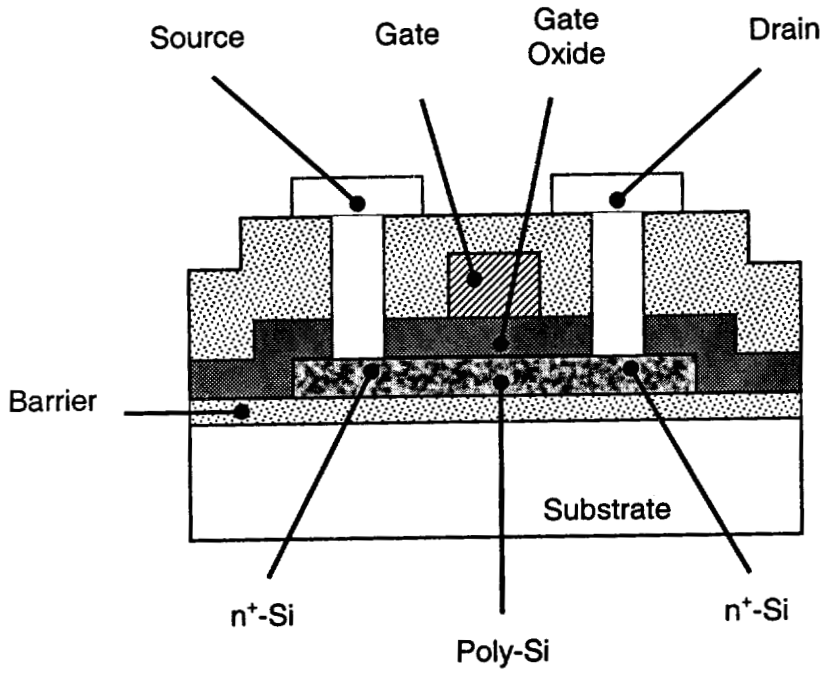

Fig.1.1: Cross section of n-MOS poly-Si TFT.

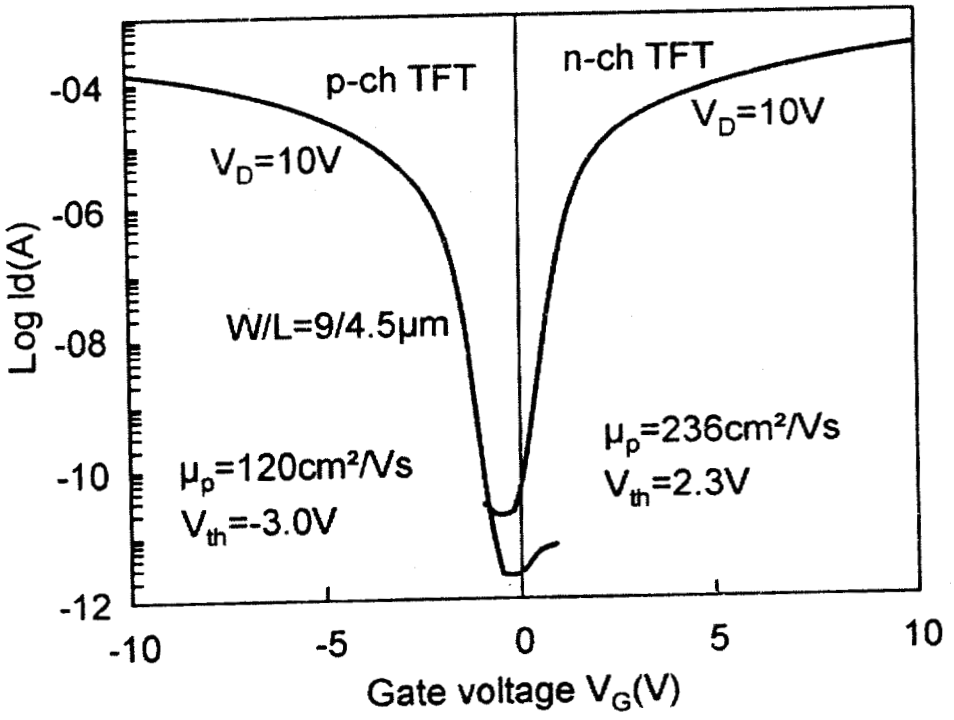

Fig.1.2: Transfer characteristics of n-MOS and p-MOS TFT [12].

1.2 Twisted Nematic LCD

In LCD application, a TFT is the switch that controls the fundamental unit of the LCD known as the picture element, or pixel, which can either transmit or block light. The pixel comprises a light source and a liquid crystal layer sandwiched between two glass plates. On each glass plate are orientation layers, electrodes and polarizers. Shown in fig.3 are the layers of the widely used Twisted Nematic (TN) LCD [12].

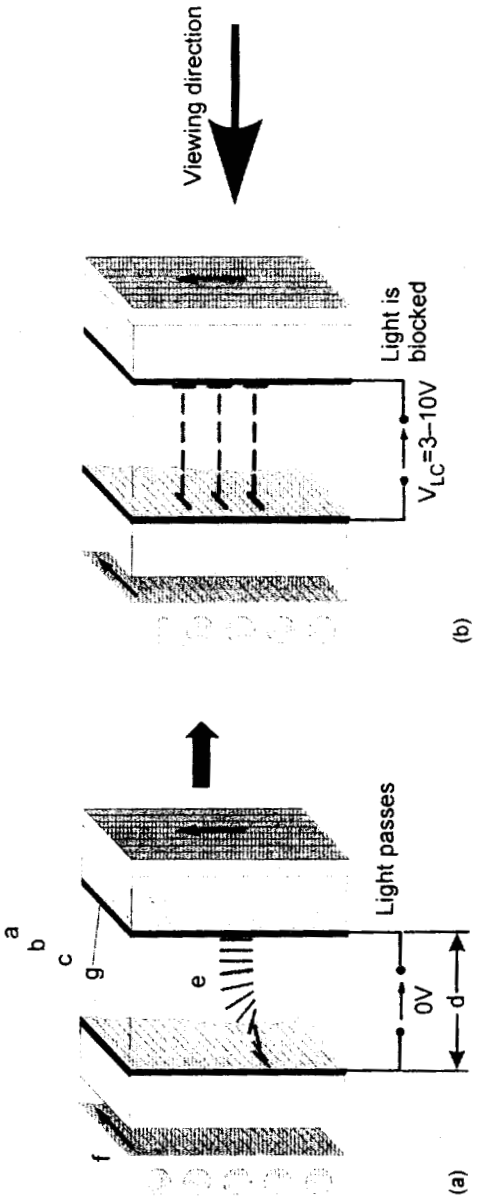

Fig. 1.3: Layers of an LCD [12].

The layers in the stack, each transparent, are as follows:

(a) Polarizer

A polarizer is a medium that changes unpolarized light into linearly polarized light. In the illustrations found here, the resulting plane of polarization is indicated by the lines in the polarizer.

(b) Substrate

In addition to being transparent, the substrate needs to be inexpensive for large-area display panel, restricting the choice of materials to the amorphous glass. This has impact on the quality of the silicon thin film deposited over it.

(c) Electrode

The electrodes are made of Indium-Tin-Oxide (ITO), a transparent conductor.

(d) Electric field

By applying voltage across the two electrodes, an electric field is set up in the liquid crystal to control. The field controls the orientation of the liquid crystal director.

(e) Liquid crystal

In this example, the liquid crystal is composed of rod-like molecules (termed calamitic). The average direction along the length of the rod is called director. The term nematic denotes crystal phase which is orientationally and positionally disordered.

(e) Light source

Light is transmitted across the layers from the back of the panel.

(g) Orientation layer

The orientation layer is a thin (e.g. 100nm) layer of organic material such as polymide with surface grooves that anchor the rod-like liquid crystal molecules. The direction of the grooves serves to orient the rod-like liquid crystal molecules. In the illustrations found here, the surface grooves are indicated by lines in the orientation layer.

In the so called normally white mode, the lines of the polarizer and orientation layer on one glass plate are parallel. The lines in the polarizer and orientation layer on the second plate are also parallel. The two polarizers, however, are crossed. Light passing

through the first plate will be linearly polarized. Without applied voltage, the liquid crystal molecules are forced by the crossed orientation layers to twist into a helix. For wavelength λ and refractive index anisotropy Δn there is a specific thickness of liquid crystal given by [12]

$$t = \frac{\sqrt{3}}{2}\frac{\lambda}{\Delta n} \tag{1.1}$$

where this twist of the molecules rotates the direction of polarization by exactly 90° degrees at the opposite side of the liquid crystal layer. This allows light to be transmitted through the stack despite the crossed polarizers, thus the term normally white mode. When non-zero voltage is applied, the liquid crystal molecules align with the direction of the electric field and will not have polarizing effect on the incoming light. The crossed polarizers then block the light. Gray shade is controlled by the magnitude of the voltage across the electrodes. The voltage applied across the electrodes is controlled by a TFT which acts as a switch for each pixel. The Active Matrix LCD is an array of pixels with TFTs as switches. With proper addressing scheme, these transistors work to produce an image by selectively turning on pixels in some places and turning off pixels in others.

1.3 An overview of polysilicon technology

Beyond the use of TFTs as switches for pixels, integration of other functionalities such as an addressing circuit onto the glass panel is desirable. For this reason, poly-Si TFT is gaining importance as such applications demand higher quality active layer. An example of the steps in a poly-Si TFT process flow listed below [13].

1. On a display grade glass, an SiO_2 or SiN_x base layer is deposited by PECVD. The layer prevents diffusion of ions from the glass into the active layer. If a quartz substrate was used, the base layer would be unnecessary.

2. 50nm thick A-Si film is then deposited by PECVD, and patterned into islands by plasma etching. To dehydrogenate the silicon film, the sample is then furnace annealed at 450°C for 2 hours in nitrogen ambient.
3. The a-Si film is treated, either in a furnace or by excimer laser irradiation, to convert it into poly-Si phase to enhance its mobility. Furnace annealing can be done in a nitrogen ambient at 600°C for 24 hours. Such prolonged heating would preclude the use of glass substrate. Irradiation by excimer laser, on the other hand, is well suited for glass substrate. Typically, the 248nm (KrF) or the 308nm laser light (XeCl) is used. The irradiation can be done in air or nitrogen ambient and the sample can be at room temperature or heated to around 400°C.
4. After the poly-Si film is patterned, a SiO_2 layer is deposited by PECVD for the gate dielectric. Next, a gate electrode material is deposited by sputtering. The gate is then patterned.
5. Implantation is done to form the source and drain regions, with the gate structure serving as mask in a self-aligned process. The sample then undergoes activation anneal using temperature of up to 400°C.
6. The last SiO2 layer is deposited by PECVD and contact holes are etched, followed by sputtering of a metal for the source and drain electrodes.

The conversion from a-Si to poly-Si is a key step in the integration of more complex circuits for expanding the functionality of the display. In this step, thermal energy is delivered to the a-Si film, allowing the atoms to reconfigure themselves so that transformation into poly-crystalline phase can result. The large grains of the poly-Si material have less grain-boundary surface area and, therefore, less traps. With less traps, carrier mobility is larger [7, 13.]. Fig 1.4 shows the improvement that annealing can achieve.

Angelis *et al.*

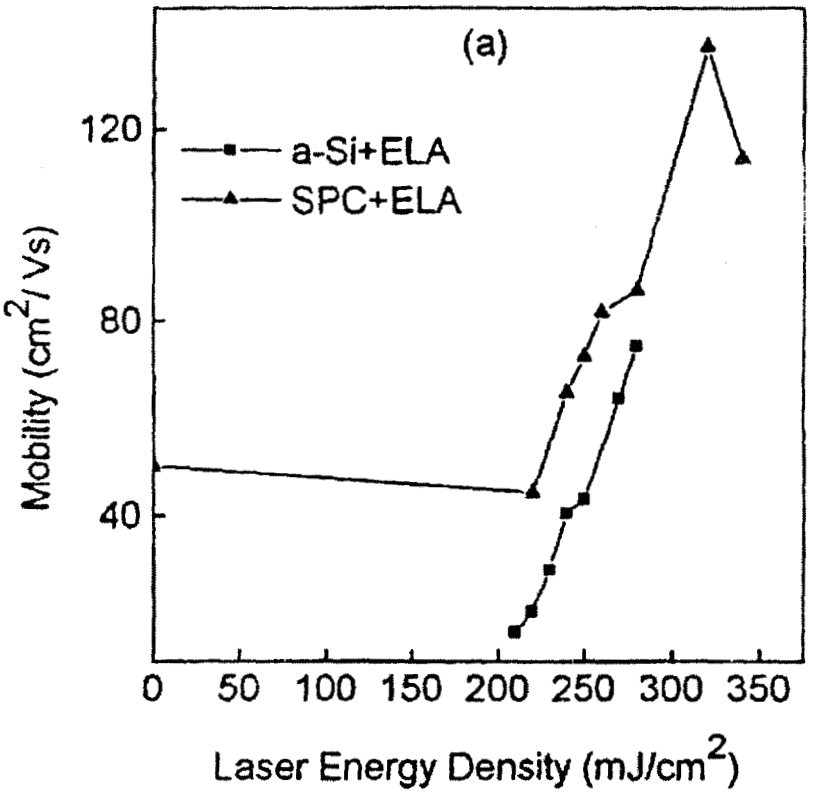

Fig. 1.4: Annealing and laser irradiation are effective means for increasing Si mobility [13].

The conversion can be achieved through solid phase crystallization (SPC) or complete melting and subsequent re-crystallization of the film. SPC occurs when a sample is subjected to high temperature (typically in a furnace), thereby transforming the a-Si into polycrystalline phase. In this case, the temperature does not cause melting and the transformation occurs in the solid phase. The range of temperatures used must be compatible with the substrate on which the film is deposited. With quartz, the temperature can be as high as 900°C but the widely used display-grade glass can not

tolerate prolonged heating beyond 600°C. This, in turn, limits the growth of the crystals. In SPC, the main parameters are time, temperature and the particular process by which the a-Si film was deposited. Essentially, the re-arrangement of atoms is proportional to the product of processing temperature and time so an increase in temperature will shorten the time needed to achieve the same effect. From throughput consideration, the process should be as short as possible. On the other hand, the temperature could not be so high as to damage the substrate. Ultimately the process is constrained by the thermal budget. In addition to the trade off between time and temperature, it has also been shown that a-Si deposition temperature and rate affects the structure of the amorphous material [14]. This in turn will affect the quality of the poly-silicon material after the annealing process.

In SPC, crystal grain size is limited by the growth rate of solid phase silicon. This means acceptable processing time (which may already be in the range of tens of hours) limits the grain size to about 1μm. Thus, efforts have been focused on enhancing the Si growth rate. To increase growth while maintaining reasonable annealing time and low enough temperature requires a catalyst. This led to Metal Induced Solid Phase Crystallization (MISPC) in which growth rate is enhanced by the free electrons of the metal and the covalent bonds of silicon [14, 15]. Further development makes use of electric field to increase Si growth rate. These are categorized as field-enhanced MISPC (FE-MISPC).

1.4 Excimer Laser Annealing/Crystallization Process

A different way to deposit energy into the silicon film was made possible by the availability of high power excimer lasers. An excimer laser has the advantage of being able to deliver a more concentrated energy to the surface of the silicon film. This means that a higher transformation temperature in the film may enhance the quality of the polycrystalline material while maintaining a lower sample temperature, making it

compatible with the glass substrates used. Unlike SPC, ELC is an ultra rapid and, therefore, highly non-equilibrium process which induces melting in the film. Here the challenge is to increase the grain size by maximizing the lateral growth (from the liquid phase) of each grain before transformation via copious nucleation takes place.

The heating is due to the strong interaction between the laser radiation and electrons in the substrate. In metal and semiconductors, electromagnetic radiation is converted into thermal energy via electronic excitation processes. Because both relaxation time for electronic excitation and electron mean free path are short, the heat is deposited where the radiation is absorbed [16]. In classical wave formulation this is expressed as the complex index of refraction and in fulfilling the boundary conditions, the solution of the wave equation has decaying amplitude, i.e. energy is absorbed. This is especially true for ultra violet (UV) light. Due to strong absorption in semiconductor, a large portion of laser energy is absorbed within only a very shallow depth below the surface of the film. The boundary conditions also require that the rest is reflected. Because a laser pulse is very short (in the order of tens of nanoseconds) its effects are localized. It causes thin film to melt but does not impart enough energy to appreciably increase the temperature of the entire sample volume. In LCD application, this is very attractive since the typical substrate may not withstand high temperature processing. For crystalline silicon substrate application, the process is used to fabricate shallow junction devices by creating very shallow molten region that would confine dopant diffusion.

In ELC, laser energy penetrates within only several nanometers from the film surface to create a melt layer bounded by a mostly planar (except at the edges) solid-liquid interface. Subsequently, the interface propagates down into the film and, depending on the fluence level, may cause complete melting in the irradiated region. There are three distinct crystallization scenarios that correspond to three fluence ranges [3, 17]. In the low fluence range, Si film is only partially melted. The melt region does not extend to the Si/glass interface and a thin, continuous layer of solid phase silicon remains below the melt region. After re-crystallization, the resulting material may then include regions transformed by explosive nucleation as well as vertical solidification. In

the high fluence range, the silicon film under irradiation is completely melted. In some regions of the melt, deep undercooling can occur in the absence of 'seed' crystals so that the phase transformation occurs via explosive nucleation, producing structure characterized by fined-grained crystals. Between the low and the high fluence ranges exists a narrow window where fluence level produces near-complete melting with isolated grains remaining at the bottom of the melt. During subsequent quenching, these grains become the seeds which will grow laterally into larger grains. Referred to as the super lateral growth (SLG) phenomenon [18], this path of transformation is crucial to producing, from liquid phase, poly-crystalline material with maximum average grain size. In this scenario, explosive nucleation between the grains is suppressed by the heat released from the moving solid-liquid interfaces. Unfortunately, SLG phenomenon only occurs within a narrow range of fluence (~50mJ/cm^2) [14] requiring high degree of accuracy and stability on the part of the laser equipment. For this reason, a trade-off must be made between process repeatability and maximum grain size.

As a refinement of the ELC process, Lateral Solidification (LS) technique exploits the super lateral growth phenomenon seen in the near-complete melting scenario but by using high fluence to induce complete melting. In the absence of isolated seed crystals, the technique seeks to extend the growth at the solid-liquid boundaries around the melt region before explosive nucleation can occur. In other words, while solidification in ELC is via the growth of isolated grains within the melt, in LS technique, solidification occurs via the lateral movement of the solid-liquid interface around the melt region. The main feature of LS technique is that the extent of melt region is commensurate to LGL so that lateral growth could form the larger part of, if not all, the solidified material. This is achieved by controlling the silicon temperature distribution in the lateral direction. Otherwise, because LGL ranges in the micrometer scale whereas the width of the melt region is typically one millimeter (same as the width of laser beam), solidification following complete melting would be dominated by nucleation. The advantage of the LS technique over conventional ELC is that process window is considerably larger, because

the usable fluence range is between the complete melt threshold and agglomeration threshold or about 200mJ/cm^2.

One implementation of LS technique utilized a mask with a narrow slit which formed an irradiation area that is several microns wide by a few millimeters long to produce a lateral growth along the direction of the short axis of the irradiation area. After the laser pulse causes the thin film to completely melt, solidification follows. During quenching, the molten region solidifies in two ways. (1) As heat dissipates and film temperature decreases, the solid-liquid interfaces that define the outer boundaries of the molten region move into the center, shrinking the molten region – solid-phase Si expands by lateral growth, one of the ways by which the film solidifies. The extent of crystallization produced in this way is termed *lateral growth length* (LGL). (2) Eventually, supercooling in the film initiates a second way of solidification where critical solid nuclei spontaneously appear in the liquid and on the Si-glass interface [19]. This is nucleation, a stochastic process. These nuclei then grow and coalesce resulting in fine-grained material in the middle of the original melt zone. An example of the two modes of crystal growth is shown in the SEM micrograph of fig. 1.5. It is desirable to suppress nucleation so that LGL is maximized. Other implementation of LS may involve patterning structures that would absorb the light and thus block some areas of the film from irradiation [14]. Provided that these structures are thick enough, areas of the silicon film underneath these structures will then be prevented from heating up and melting, thus limiting the extent of the melt region.

As stated earlier, it is desirable to suppress nucleation so that LGL is maximized. A physically consistent simulation can point to how this can be achieved. The model, however, needs to take into account both paths of solidification. In this investigation, such a model was developed. Simulations based on the model yields a wealth of information that includes temperature evolution, solid-liquid interface velocity, nucleation statistics and LGL, all of which are useful in determining the optimal conditions of laser re-crystallization. When the beam is narrow enough (after passing through the narrow slit of a mask) it is possible to produce complete lateral solidification

across the irradiation area. The beam can then be translated by a distance less than the lateral growth length, so the next irradiation will create a new melt region adjacent to the first laterally grown region. During quenching, the crystals in the laterally grown region provide the seeds for the transformation in the second melt region. This is then repeated to extend the laterally grown region ad infinitum. Developed by Im and coworkers at Columbia University, this process was termed Sequential Lateral Solidification (SLS) [20]. In theory, the size (of one axis along the scan direction) of the crystalline grain can be as large as necessary. For continuity, it is crucial that translation distance is commensurate to the LGL. For this reason, LGL is a key attribute for characterizing and evaluating laser solidification process. The focus of the development of the ELC model in this work was to simulate one irradiation cycle of the SLS process.

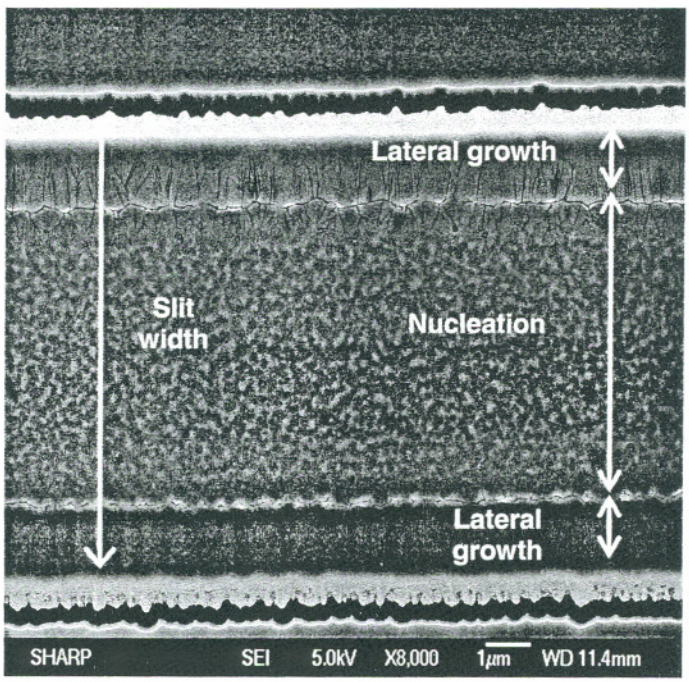

Figure 1.5: SEM photograph (planar view) of a 100nm-thick Si film irradiated with a 10μm-wide XeCl beamlet at a laser fluence of 486mJ/cm^2. Laterally-grown and nucleated regions have been marked on the photo.

The idea of inducing complete melting to produce an amount of lateral growth at one location and then translating the beam to extend the lateral growth region had been further developed as a mean to control the location of grain boundaries [21, 22]. By using specially designed mask (e.g. chevron shaped), 'large' area of the amorphous film can be converted into a single crystalline material [23]. These developments represent some of the most promising techniques for polysilicon materials to date.

Laser annealing is advantageous because it can achieve localized heating. In ELC, prolonged and excessive heating can be avoided because pulse duration is very short. For practical purpose, the substrate temperature is largely unaffected, making the process compatible with glass substrates. However, even with techniques where large single crystalline silicon is produced, there remain two issues. The first has to do with grain boundaries that are located in the channel of the device. As devices shrink and poly-crystalline grain size increase, the statistical variation in the device electrical characteristics increases. Instead of containing a large number of grain boundaries with various orientations (as in the case of a-Si) poly-Si films contain fewer grain boundaries. If these boundaries are electrically active, the large difference in the material structure of the devices will degrade the uniformity of device characteristics [24]. For this reason, techniques that afford some control over the positioning of these grain boundaries are important. The ability to predict LGL can help in this direction and, therefore, simulation capability that accounts for undercooling and lateral growth becomes necessary. The second has to do with intra-grain defects generated by the high quenching rate induced by ELC. In the highly non-equilibrium environment of ELC, the short time in which solidification takes place does not allow perfect rearrangement of the atoms. Because of the complex thermal gradients and mechanical stresses that are present, defects (e.g. twins) are generated. Also, because of the volume expansion that occurs during solidification of Si, hillocks or ridges form where two laterally grown regions meet [7]. Even without the capability to account for the generation of intra-grain defects or the formation of ridges a model that accounts for interface velocity and quenching rate could qualitatively explain how such defects are generated.

1.5 Review of Past Experiments

The following sections present past investigations in the two topics of nucleation and modeling of laser annealing. Modeling of laser annealing depends on results from the investigations of nucleation phenomena since an accurate model must include nucleation. The model also needs to incorporate the nucleation rate which is the focus of the first group of works presented here.

1.5.1 Nucleation rate experiments

The phenomenon of supercooling is where a material remains in its liquid phase even at temperatures below equilibrium freezing point. The Classical Nucleation Theory (CNT) attributes this to the existence of an energy barrier that needs to be overcome in the creation of the solid phase nucleus (precursor of solidification). It asserts that the creation of a nucleus is fundamentally a random process. However, once a nucleus appears, two opposing forces act on it: free energy of formation that favors its growth and surface energy that favors minimizing its surface area. The superposition of the two forces results in a critical energy, a barrier to be overcome by the nucleus, beyond which its growth is ensured. The macroscopic manifestation of this energy barrier is the nucleation rate. CNT relates nucleation rate, a function of temperature and time, to the energy barrier for nucleus growth. This provided the motivation for experiments that were designed to measure the degree of supercooling and from which nucleation rates were derived.

The model developed in this work includes nucleation rate as one of its key input parameters and, for this reason, a discussion of past experiments done to measure nucleation rate is pertinent. They involve the controlled heating of known quantity of materials. Each material melts and then quenched to temperatures below their equilibrium

freezing points. Throughout this time, temperature of the material and duration in which a material remains in liquid phase are monitored. The degree of supercooling is obtained by observing the temperature at which nucleation occurs. Based on these, nucleation rate can be derived.

Nucleation rate is a function of kinetic prefactor (I_{0a} and I_{0v}), surface energy (σ), energy barrier to nucleation (ΔG_{ls}) and contact angle (θ) characterizing the catalytic surface that is present. Kinetic prefactor is well established from experiments designed to specifically measure it. Surface energy and energy barrier can also be obtained from specific experiments. By assuming certain values for kinetic prefactor, surface energy and energy barrier, contact angle can then be determined by curve fitting as done by Leonard [25].

Devaud and Turnbull [26] used melted uncoated Si droplets (0.4mm – 0.8mm in diameter) and found that they could be undercooled by 250°C. They also melted uncoated Ge droplets (0.4 mm – 0.8mm in diameter) in B_2O_3 flux and undercooled them by 280°C. Temperature of Si droplet was measured by Rh thermocouple. Melting was observable as change of reflectivity that occurs (visible by naked eye). The onset of crystallization was observed as a flash of light due to the release of latent heat. Since the droplet volume and time of the onset of nucleation was known, by assuming single nucleation event the upper limit of the homogenous nucleation frequency was determined (whether the nucleation was homogenous or heterogeneous cannot be proven).

This experiment was one of many variations of droplet experiments. The improvements in droplet experiments were in the ways the droplets were maintained in environments that would suppress heterogeneous nucleation. Shown in Fig. 1.6 are several methods to suppress heterogeneous nucleation are (a) fluxing, (b) drop column, (c) levitation and thin film islands. The results of such experiments are summarized in Table 1.1.

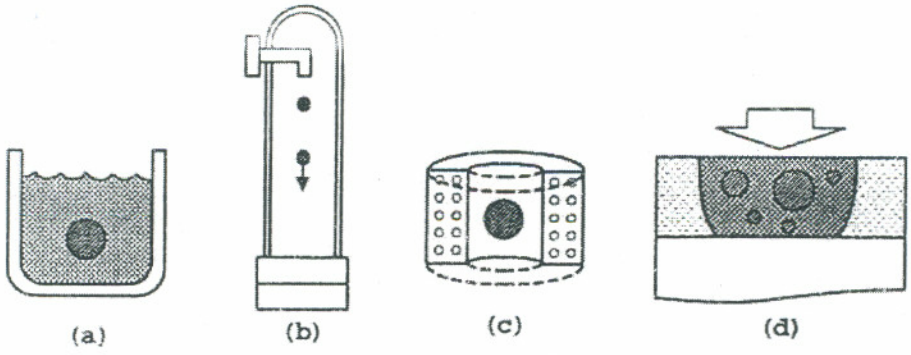

Fig. 1.6: Schematic of experimental methods used to measure nucleation rate [25].

Table 1.1: Summary of nucleation rate experiments on silicon.

Investigator	Method	ΔT (K)	$\text{Log}_{10} I$	σ (J/m^2)
Devaud & Turnbull [26]	Droplet	240 ± 20	10.30	0.34
Stiffler & Thompson [27]	Droplet	505 ± 40	29.00	0.34
Spaepen & Shao [28]	Droplet	350 ± 10	9.59	0.38
Im & Song [29]	Silicon islands	--	--	--

To measure nucleation rate Im et al devised a unique method that yield important result [25]. Instead of using individual droplets of Si, Im et al patterned an array of Si islands of equal volumes using standard photolithography and dry etch process. In this

experiment, a thin a-Si film is deposited over an SiO_2 layer. The Si film was patterned to create an array of uniform Si islands which were then encapsulated by another layer of oxide. The sample was then irradiated and quenched. When it re-crystallized, nucleation in one island did not affect the neighboring islands. As nucleation spontaneously occurs in the islands, the population of liquid islands decayed in time with the decay constant being equal to the nucleation frequency. The population of liquid islands during solidification was derived from the surface reflectivity (measured in-situ) of the film. Assuming that re-crystallization in an individual island is due to single nucleation event, by plotting reflectivity as a function of time the nucleation frequency can be extracted (see fig. 1.7 below).

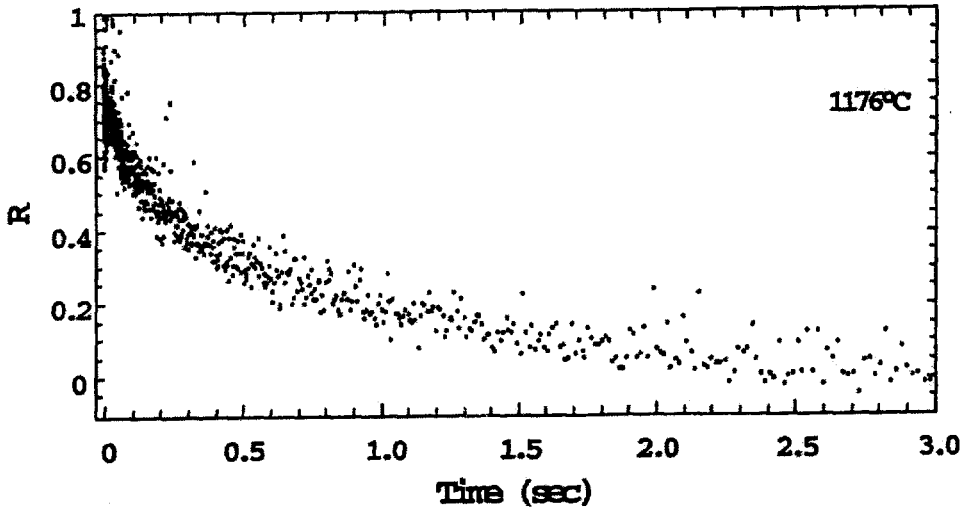

Fig. 1.7: The decay constant of the reflectivity vs. time curve is the nucleation frequency [25].

The advantage of this method is its accuracy, both due to the timescale used and its statistical nature since, in effect, hundreds of experiments are done simultaneously. Also, this experiment was able to approach isothermal conditions desired due to better temperature control.

1.5.2. Modeling of laser anneal process

One of the first applications of laser re-crystallization process was for eliminating lattice damage from ion implantation. Such process resulted in shallow melted region near the sample surface. It was assumed that the process starts with the solid-liquid interface moving deeper from the surface into the sample followed by the return of the interface to the surface during subsequent quenching. The movement of solid-liquid interface implies liquid phase epitaxy.

Baeri et al modeled such laser re-crystallization process by developing a one dimensional model to simulate the transformation from an ion-implanted amorphous layer to single crystal Si by liquid phase epitaxy [30]. The irradiated area was large enough so that temperature variation across the sample surface was ignored and only variation along the depth of the sample was of interest. The solution of the heat equation was found by an unspecified numerical method. The model assumed that phase change occurs at equilibrium melting point. Experiments were done on samples with amorphous layers with thickness of 500Å to 9000Å. To anneal the samples, Q-switched ruby laser ($\lambda = 0.69\mu m$) was used. The energy used was 0.2 J/cm^2 to 3.5J/cm^2 with pulse duration of 20ns and 50ns. The main interest was to determine thickness-energy-density threshold to achieve surface melting. The limitation here is not only that this is a one dimensional model, but also in its assumption that phase change occurs at equilibrium melting temperature.

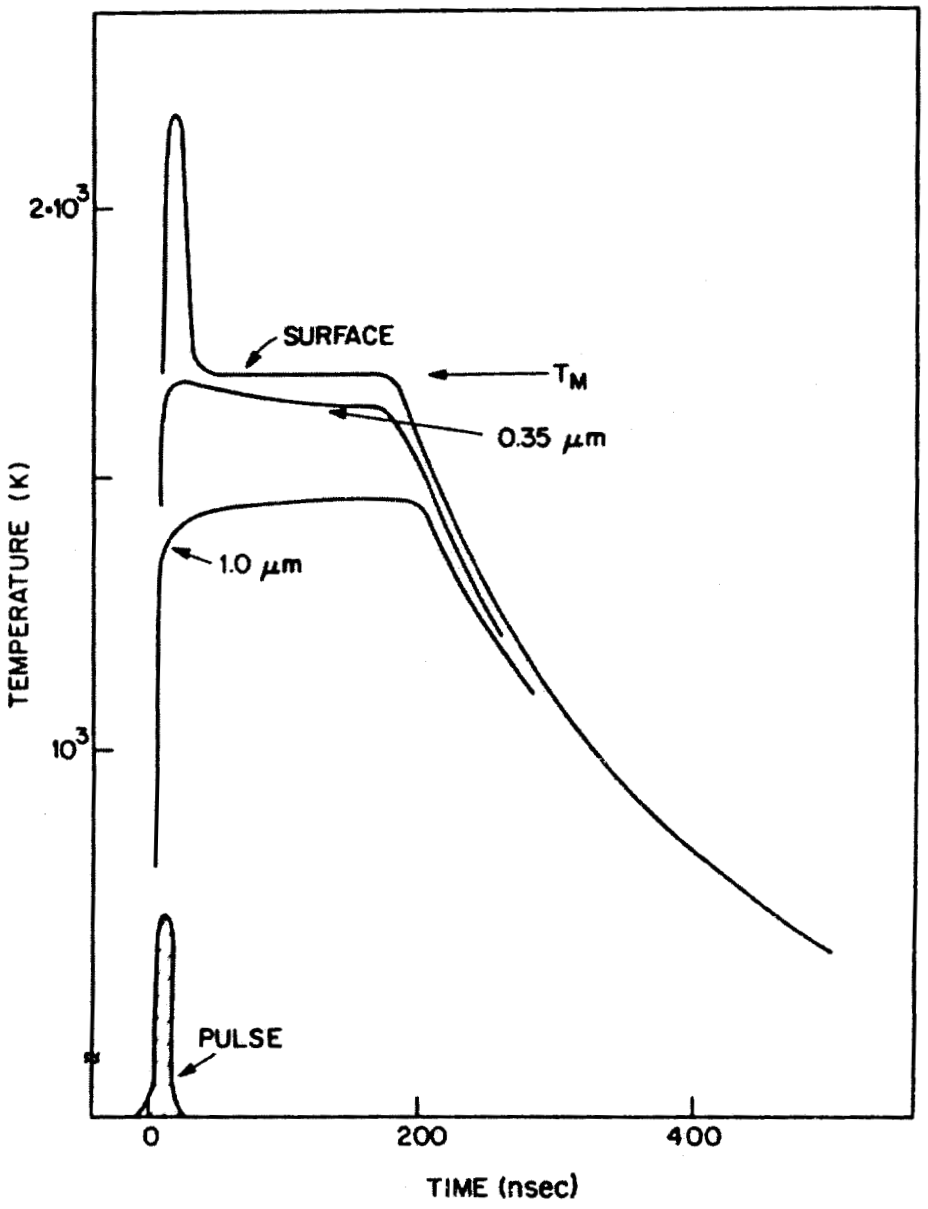

Fig 1.8: An example of equilibrium approach resulting in plateau at equilibrium melting temperature, T_m [11].

Using finite-difference method, Wood and Giles developed a one dimensional model to simulate the heat and mass transport that occurs during implant-anneal process [9]. Their interests were among others, to determine the maximum depth of the melted region, duration of surface melting as well as final dopant distribution to explain the experimental results obtained. Again, because similar assumption was made regarding phase change, the approach is not adequate.

Unlike previous applications for implant anneal, Gupta et al modeled ELA processing of a thin layer of amorphous silicon [31]. In this case, the film was completely melted and re-solidified in a different way than in the case of implant anneal. A two dimensional model was required to account for the solid-liquid interface moving in from the boundary of the melted region as well as the heat dissipation into the sample depth. To solve the heat equation, the alternate direction finite difference method was chosen.

The key difference to the previous method was that instead of using the equilibrium formulation, it assumed that solidification only occurred at the solid-liquid interface and that the liquid could be supercooled. It is also assumed that the rate of solidification was determined by an interface response function that relates the interface velocity to the degree of supercooling at the solid-liquid interface, or in other words, the interface supercooling is what drives the interface. This approach accounts for the existence of a sharp liquid-solid interface and supercooling.

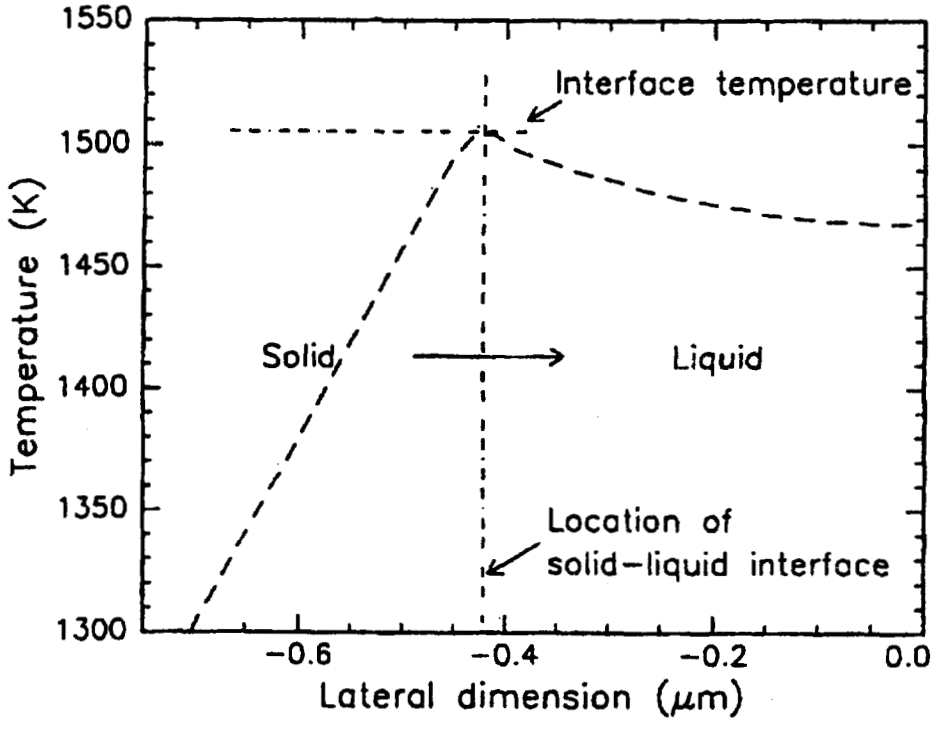

Fig 1.9: Temperature profile of irradiated domain shows the location of a sharp solid-liquid interface where temperature is highest due to solidification at the interface and the resulting latent heat [31].

Building on Gupta's work, Leonard developed a three dimensional model for laser re-crystallization of thin amorphous silicon film using the alternate direction finite difference method [25]. To simulate crystal growth in three-dimensional space, he used cellular automata formulation. An additional algorithm was developed to simulate random nucleation. The algorithm is based on a Monte Carlo process which compares the value of a deterministic probability function with a randomly generated value to simulate the random formation of critical solid nucleus. Once the nucleus has appeared, the crystal growth was taken care of by the cellular automata algorithm.

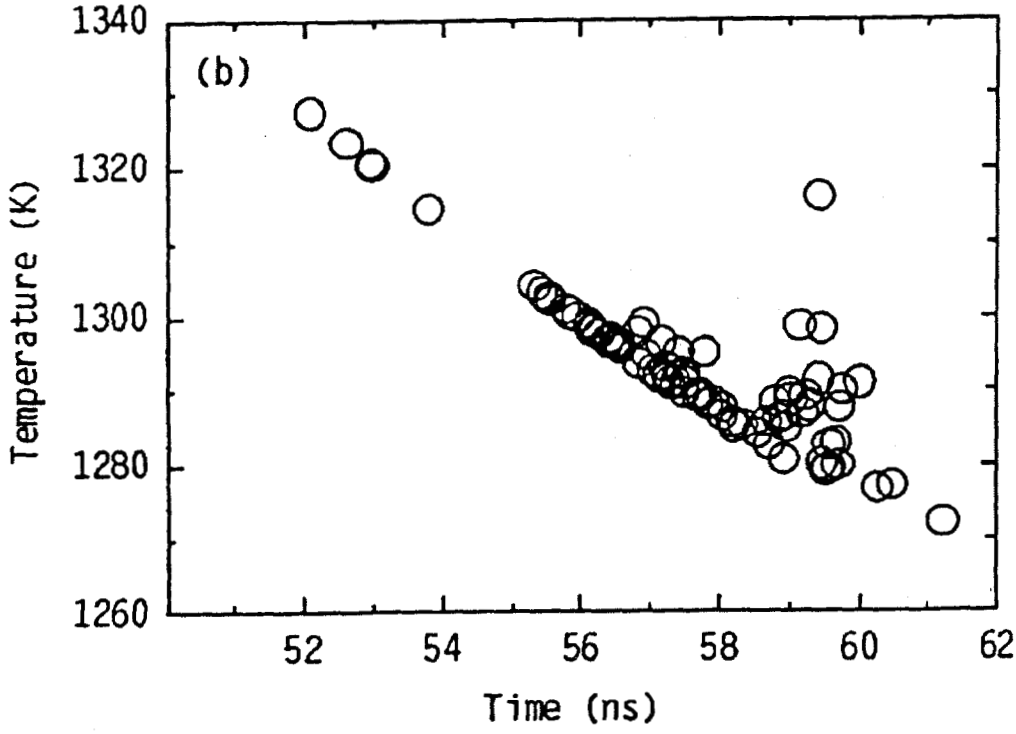

Fig 1.10: A distribution of nucleation temperatures and times obtained from a simulation illustrates the random nature of nucleation [25].

1.6 Motivation and Approach

Unfortunately, most of the works outlined above do not correctly portray the ELC process. An exception to this is the work by Leonard and co-workers [31, 32], which was adapted for the Alternate-Direction Finite Difference method. A flexible and user friendly tool for modeling the ELC process is needed. Furthermore, the sensitivity of LGL to key thermo-physical parameters has not been determined. Also, more complex ELC processes (e.g. involving multiple beams) need to be explored and their process window need to be

determined. Based on an algorithm developed by Leonard and coworkers, we believe that our work is the first implemented for use with a finite-element method (FEM) that can answer the concerns mentioned.

The approach taken in this investigation was to select an available FEM analysis tool and develop a model that would enable the tool to simulate the ELC process. The aim was to develop a tool that was user friendly, robust yet flexible to support future research. To simulate ELC, the model must take into account phase transformation that occurs only at non-diffuse solid-liquid interfaces as well as solidification through random nucleation in a supercooled liquid, i.e., phase change that is driven by kinetics, not thermodynamics. The model must have the capabilities to (1) track liquid-solid interface, (2) simulate random nucleation and (3) be adapted to the chosen FEM analysis tool for ease of use and flexibility. Also the parameters used in the simulations need to be close to published values and that simulation results match our experiments. For this a unique set of rules were developed to produce similar capabilities attained by Leonard's cellular automata algorithm. Once the model is verified, the effects of key thermo-physical parameters need to be studied. Another aspect of the ELC process that was studied was how beam shape affected lateral growth length and other ways in which lateral growth length can be maximized and maximum film temperature minimized.

In problems involving heat transfer, the governing equation is the well known heat equation (eq. 1.2) as derived from the principle of energy conservation. In modeling the ELC process, the model applies two energy sources to cause temperature change in the film. These energy sources represent (a) laser energy, S_{Laser}, and (b) latent heat of phase, $S_{\Delta\text{Hm}}$, change in the heat equation

$$\rho c_p \frac{\partial T}{\partial t} = \frac{\partial}{\partial x}\left(k\frac{\partial T}{\partial x}\right) + \frac{\partial}{\partial y}\left(k\frac{\partial T}{\partial y}\right) + \frac{\partial}{\partial z}\left(k\frac{\partial T}{\partial z}\right) + S_{\text{Laser}} + S_{\Delta H_m} \qquad (1.2)$$

where ρ is the density, c_p is the specific heat and k is the thermal conductivity of Si and T is the absolute temperature. The main task of the model is to compute the two energy sources in the above equation. At each time step the model is called to compute the laser

energy absorbed (S_{Laser}) and to determine which cells undergo phase change and to compute the latent heat that is released or absorbed ($S_{\Delta Hm}$). With the energy sources determined, we could then solve for T by using FEM.

The laser energy term can be computed since coefficient of absorption, α, and reflectivity, R, are well established for amorphous silicon film. The physical meaning of these two parameters is explained in Chapter 2. Other inputs for the model describe the incoming laser energy as a function of both temporal and spatial domains so that realistic beam profiles can be accurately represented.

While the treatment of laser energy source is straightforward, the treatment of latent heat is challenging. Phase change only occurs either at the advancing/retreating solid-liquid interface or wherever a solid phase critical nucleus appears. This means that away from the interface, the liquid phase persists with temperatures well below the equilibrium melting point (supercooling) until a solid-phase critical nucleus appears. This is unlike the thermodynamic formulation, where phase change occurs whenever the equilibrium melting temperature is reached. A key feature of this model is its capability to follow/track the position of the liquid-solid interface. This is crucial because the liquid-solid interface is where phase change occurs and its movement determines where and how much latent heat is absorbed or released at any time.

In addition to tracking solid-liquid interfaces, the model needs to simulate random nucleation. The model must determine when and where nucleation occurs because nucleation creates new solid-liquid interfaces which later propagate as the nucleated solid grows. To simulate random nucleation, a Monte Carlo based algorithm adapted by Leonard and Im [33] is used. One element of the algorithm is the probability function $P_{liquid}(T, t)$ which computes the probability of each cell avoiding a nucleation event (and thus remains in liquid phase) as a function of time and temperature. Derived from classical nucleation theory (CNT) and homogeneous Poisson statistics, $P_{liquid}(T, t)$ for heterogeneous nucleation, for example, is given by:

$$P_{\text{liquid}}(T,t) = e^{(-I_a(T)\,at)} \tag{1.3}$$

where a is the area of Si-glass interface bounded by the cell and $I_a(T)$ is the heterogeneous nucleation rate. In turn, $I_a(T)$ is a function of the free energy of formation, (ΔG_{ls}), and the surface energy (σ), as well as the contact angle (θ), given by

$$I_a(T_{i,t}) = I_{oa}(T_{i,t}) \exp\left[-\frac{16\pi\sigma^3}{3k_B T_{i,t} \Delta G_{ls}(T_{i,t})^2} \cdot f(\theta)\right] \tag{1.4}$$

where, k_B is Boltzmann's constant and I_{oa} is a kinetic prefactor.

The second part of the algorithm is a random number generator that gives a unique number to each element at each time step Δt. This number is then compared to $P_{\text{liquid}}(T, t)$. When the number is larger than $P_{\text{liquid}}(T, t)$, nucleation is said to occur within the element. As the probability decays in time or as the temperature decreases, nucleation will be more and more likely to occur.

In order to verify the validity of the model, simulations were run and their results compared with experimental data. We annealed samples with 30nm, 50nm and 100nm thick amorphous Si films using a range of laser fluences to completely melt the film and characterized the trend of LGL vs. fluence. The goal was to obtain a match using realistic/established thermo-physical parameters. Furthermore, simulations were run to show the sensitivity of the LGL to the various parameters. If the simulations matched the experimental data, we can then be confident of the reliability of the model.

The model can then be used to simulate unconventional processes such as those involving multiple beams. Ultimately it is desirable to study how ELC process can be optimized to obtain maximum LGL. There is pressing need for this since tailoring laser profiles require extensive hardware modifications or at the least a distinct set of mask. It is anticipated that the simulations can point to and explain the merits of certain schemes with regards to maximizing LGL. Such a model can be invaluable in exploratory investigations prior to designing laborious or expensive experiments. The model also has

the flexibility to simulate different film stacks as well as multiple pulse schemes with realistic laser beam profiles. The understanding afforded by such simulations can point to optimal process window in terms of not only LGL but also film temperature and solidification velocity.

1.7 Organization of dissertation

This body of this dissertation is organized into 3 chapters:

Chapter 2 reviews the theoretical foundations on which our work was based and presents key principles of ELC process. Starting with the absorption and reflection of light by semiconductor, it continues to discuss the melting and subsequent supercooling of silicon thin film. A brief overview of liquid phase epitaxy and Classical Nucleation Theory is presented as two ways by which thin silicon film re-crystallizes.

Chapter 3 presents the model that has been developed to accurately simulate the ELC process. The advantage of cellular automata approach is explained and the algorithm is described. The description of the simulation capability is presented. Examples of simulation output are analyzed and interpreted. The simulation and experimental results are compared.

Chapter 4 presents the results of the sensitivity study done to examine the behavior of the model as a function of a set of key variables. A method for approximating process window for multiple beam process is advanced. Simulation results of multiple beam process are analyzed. This presentation then concludes by a discussion on the effects of various thermo-physical parameters used in the simulation. It also points to direction for future works.

CHAPTER 2: THEORETICAL BACKGROUND

This chapter presents the theoretical concepts on which the model described in Chapter 1 is based. The model's key function is to provide the FEM analysis tool with volumetric energy source terms for each element in the domain for each time step in the course of a simulation. The model needs to consider two distinct types of energy sources. One energy source represents the laser energy absorbed in an element. Another represents the energy released or consumed by phase change in cases where a solid-liquid interface is present in the element. The model is based on the following principles:

(a) Theory of strong absorption and reflection of electro-magnetic radiation at a boundary between two media for predicting how laser energy is absorbed by a thin film [34].

(b) Theory of phase transformation at the solid-liquid interface for simulating grain growth and tracking the movement of solid-liquid interfaces. The transformation mechanism at the moving solid-liquid interface is the key for computing the magnitude and position of the latent heat source terms [35, 36].

(c) Classical nucleation theory (CNT) and pseudo-random number generator for simulating random nucleation. The model must account for the occurrence of nucleation which, in forming a new solid-phase nucleus, creates new solid-liquid interface that bounds the new nucleus [37, 38, 39].

2.1 Strong absorption and reflection in metals

ELA is a process in which excimer laser delivers the energy needed to modify a material. The use of ultra-violet (UV) laser on thin silicon film results in high concentration of energy being absorbed by the thin film which causes it to melt. On the other hand, the total amount of energy in the laser pulse is small when the entire sample volume (thin film and substrate) is considered so the process leaves the bulk of the sample without appreciable increase in temperature. Silicon is a strongly absorbing media in the UV range of wavelength (including λ = 308nm). Beyond the distance of few tens of nanometer, the amplitude is completely attenuated. Some of the energy is absorbed in the form of heat and the rest is reflected. This is simulated by the model using the absorption coefficient α and reflectivity R to compute laser source term as a function of depth from the film's surface.

To explain the physical meaning of the absorption coefficient α and reflectivity R, we begin by treating laser radiation as a plane wave, i.e., with electro-magnetic field varying in only one direction. In rectangular coordinates, we will take this to be along the z direction. Consider then the Maxwell equation

$$\nabla \times \overline{E} = -\mu \frac{\partial \overline{H}}{\partial t} \tag{2.1}$$

where $\overline{E}$ and $\overline{H}$ are electric and magnetic fields respectively, μ permeability of the medium and t is time. The equation predicts the propagation of a wave because it yields a one dimensional wave equation

$$\frac{\partial^2 E_x}{\partial z^2} = \mu\varepsilon \frac{\partial^2 E_x}{\partial t^2} \tag{2.2}$$

where E_x is the electric component in the x direction and ε is the permittivity of the medium. The one dimensional wave equation has a solution in the form of a function that propagates in the z direction with the velocity v:

$$v = \frac{1}{\sqrt{\mu\varepsilon}} \tag{2.3}$$

In the case of laser annealing the laser beam propagates through two media: vacuum and silicon. We can take the boundary to be parallel to the X-Y plane (see fig. 2.1).

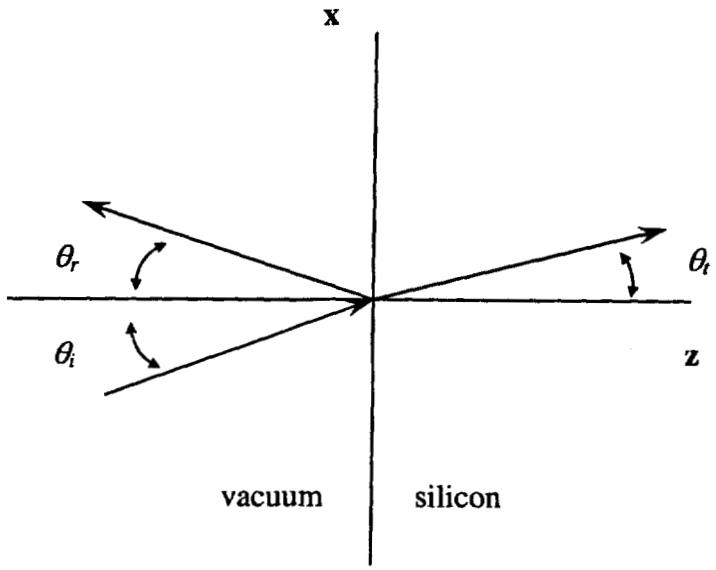

Fig. 2.1: Reflection and transmission of light wave at the interface between two media. The symbols *i*, *r* and *t* denote incident, reflected and *t* transmitted wave, respectively.

As mentioned above, light is completely attenuated within the film. In semiconductor such as silicon, some of the energy is absorbed by electrons in band-to-band transition. In the subsequent relaxation, the energy is imparted to the lattice in the form of heat while the rest is reflected. We then have incident wave, transmitted wave and reflected wave. In the figure above, *i* is incident wave, *r* is reflected wave and *t* transmitted wave.

As with metals and molten silicon, the strong absorption can be seen as the result of the interaction between the electrons in the material which behave as damped oscillators when subjected to resonance frequency. Thus the absorbed energy of the transmitted wave is dissipated as heat, causing the temperature of the metal to rise. In the case of normal incidence (angle $\theta_i = 0$), the power of the wave decays as it penetrates into the material and is given by:

$$F(z) = F_0 e^{-\alpha z} \tag{2.4}$$

For 308nm wavelength, established value of the absorption coefficient, α, is $2 \cdot 10^6 \text{cm}^{-1}$. Inside the medium, the wave then be represented by

$$E_x(z) = A_0 \exp\{-\alpha z + i(\omega t - kz)\} \tag{2.5}$$

and if we use $\chi = \alpha/k$ and $n = kc/\omega$ we can rewrite (2.5) as

$$E_x(z) = A_0 \exp i\omega\{t - \frac{n^*}{c} z\} \tag{2.6}$$

Here ω is the angular frequency, n^* is the complex index and c is the speed of light. Furthermore, when light passes from one medium into another, boundary conditions specify how solutions to field equations such as (2.1), valid on one side of the boundary, fit with solutions at the other side. For waves at optical frequency, the following boundary conditions apply:

$$E_{1x} = E_{2x}$$

$$H_{1x} = H_{2x}$$

$$D_{1z} = D_{2z}$$

$$E_{1y} = E_{2y}$$

$$H_{1y} = H_{2y}$$

$$H_{1z} = H_{2z}$$

Applying the boundary conditions, the wave equation solution in vacuum is a combination of the incident wave

$$E_i(z,t) = A_i \exp i\omega\{t - \frac{1}{c}(x\sin\theta_i - z\cos\theta_i)\} \tag{2.7}$$

and the reflected wave

$$E_r(z) = A_r \exp i\omega\{t - \frac{1}{c}(x\sin\theta_r + z\cos\theta_r)\} \tag{2.8}$$

For normal incidence we get the following expression for the ratio of the reflected to the incident energy:

$$\rho = \frac{n-1}{n+1}\cdot\frac{n^*-1}{n^*+1} \tag{2.9}$$

We can then translate this into reflection coefficient R (for 0° angle of incidence) which we use to compute the laser energy absorbed in the film. For λ = 308nm, the accepted value of R is 0.6. Together with the absorption coefficient α we can then compute source term as a function of depth in the film. In a slice of material with thickness of Δt at depth of z, the energy absorbed by the slice is

$$(1-R)\cdot ED\int_{t-\Delta t}^{t+\Delta t}\exp\{-\alpha t\} \tag{2.10}$$

where *ED* is energy density, in $J \cdot cm^{-2}$ and *R* is reflectivity. Laser source term decays within the film as shown by fig 2.2.

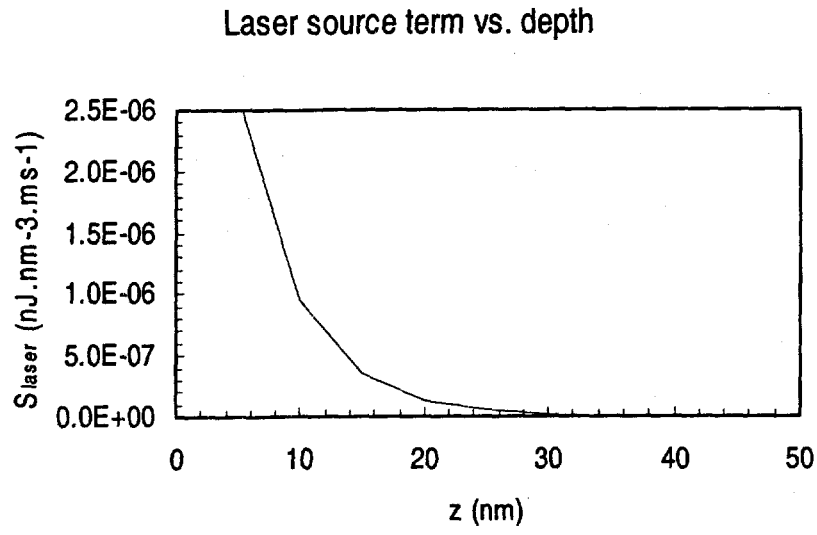

Fig 2.2: Laser energy is absorbed within the film and converted into thermal energy through its interaction with the film. The volumetric source term representing such coupling between light and matter decays with depth.

2.2 Transformation at solid-liquid interface and interface response function

The movement of a solid-liquid interface constitutes the transformation between liquid and solid phases. Phase transformation is an atomistic process, where atoms/molecules move across the interface between two regions of different phases. In solidification, there is a net flux of atoms/molecules crossing over from the liquid to the solid region. These molecules then attach themselves onto the solid surface and decrease

their free energy. This results in the expansion of the solid domain or, equivalently, the displacement of solid-liquid interface from which latent heat is released.

In the context of tracking such solid-liquid interface, the so-called interface response function (IRF) is a key part of the model. Solid-liquid interface velocity is a function of the degree of undercooling at the interface, as defined by the IRF. In other words, it is deviation from equilibrium melting temperature that drives the solid-liquid interface. The model uses the IRF and temperature data to determine the displacement or translation of the interface within a particular time step. To understand the dependence of the normal interface velocity of the planar interface on undercooling, we begin by considering the energy barrier that a molecule needs to overcome as it crosses over from the liquid to the solid region [35]. This energy barrier is referred to as ΔG_t^* or the activation free energy, as shown in fig 2.3 (a, b).

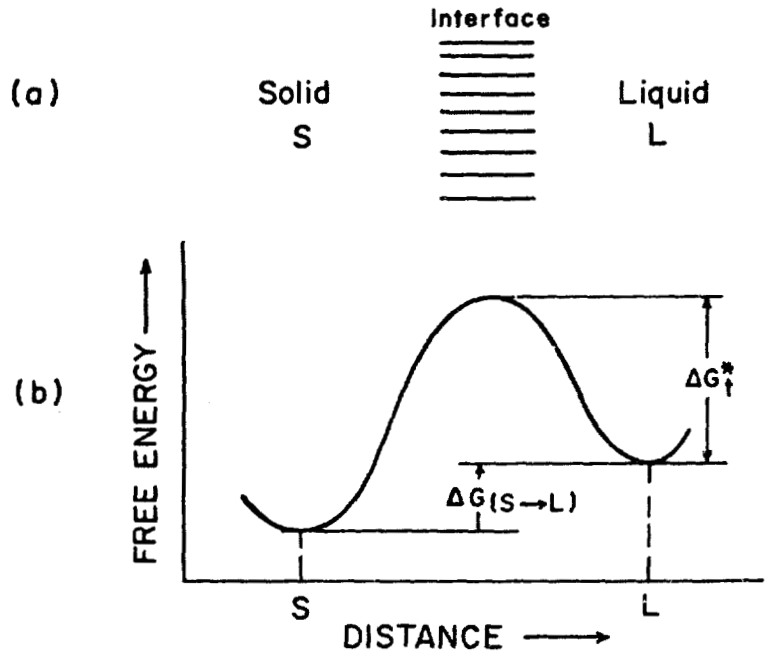

Fig 2.3: The liquid and solid phase regions is separated by energy barrier that must be overcome by a molecule crossing between the two regions. This energy barrier is referred to as ΔG_t^* or the activation free energy of transformation [35].

The flux of molecules going across the interface from liquid to solid phase, $J(L \rightarrow S)$, is given by

$$J(L \rightarrow S) = n_L f_S \nu_L \exp\left\{-\frac{\Delta G_t^*}{kT}\right\} \tag{2.11}$$

where n_L is the number of molecules in the liquid which face a unit area of the interface, f_S is the fraction of molecules that attach themselves (fraction adsorbed) onto the solid surface after crossing over, ν_L is the molecule's (liquid phase) vibration frequency at the interface, ΔG_t^* is the activation free energy which the molecules must acquire to jump across the interface, and T is the absolute temperature. Similarly, the flux of molecules from solid to liquid, $J(S \rightarrow L)$, can be written as

$$J(L \rightarrow S) = n_S f_L \nu_S \exp\left\{-\frac{\Delta G(S \rightarrow L)/N + \Delta G_t^*}{kT}\right\} \tag{2.12}$$

The net flux can then be written as

$$\begin{aligned} J_{net}(L \rightarrow S) &= J(L \rightarrow S) - J(S \rightarrow L) \\ &= \exp\left\{-\frac{\Delta G_t^*}{kT}\right\}\left\{n_L f_S \nu_L - n_S f_L \nu_S \exp\left[-\frac{\Delta G(S \rightarrow L)}{RT}\right]\right\} \end{aligned} \tag{2.13}$$

Taking $n_L \approx n_S = n$, and $\nu_L \approx \nu_S = \nu$ and $f_L = 1$ we have

$$J_{net}(L \rightarrow S) = n\nu \exp\left\{-\frac{\Delta S_t^*}{k}\right\}\exp\left(-\frac{\Delta H_t^*}{kT}\right)\left\{f_S - \exp\left[-\frac{\Delta G(L \rightarrow S)}{RT}\right]\right\} \tag{2.14}$$

where ΔS_t^* is the activation entropy and ΔH_t^* is the activation enthalpy. The rate of inclusion/adsorption can be seen as the velocity of the interface, thus the solid's growth rate $\dot{G}$ is the product of the solid's molecular volume, V_S/N, and the net flux, $J(L \rightarrow S)$

$$\dot{G} = \left(\frac{V_S}{N}\right) n\nu \exp\left\{-\frac{\Delta S_t^*}{k}\right\}\exp\left(-\frac{\Delta H_t^*}{kT}\right)\left[1 - \exp\left\{\frac{\Delta G(L \rightarrow S)}{RT}\right\}\right] \tag{2.15}$$

At temperatures close to T_m, an expansion of $\exp[\Delta G(L \rightarrow S))/RT]$ reduces eq. 2.15 reduces to

$$\dot{G} = \left(\frac{V_S}{N}\right) n\nu \exp\left\{-\frac{\Delta S_t^*}{k}\right\} \exp\left(-\frac{\Delta H_t^*}{kT}\right)\left[\frac{-\Delta H(L \rightarrow S)(T_m - T)}{RTT_m}\right] \tag{2.16}$$

Because ΔH_t^* has the same order of magnitude as the activation energy for diffusion in liquids (very small in the case of metals), near T_m growth rate can be approximated with a linear function of undercooling, T_m - T. The growth rate $\dot{G}$ is plotted in fig. 2.4 below

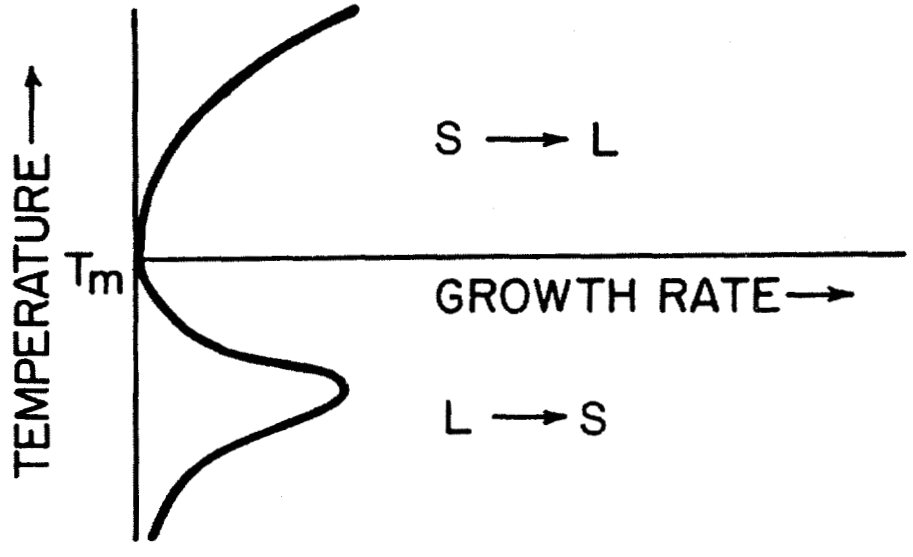

Fig. 2.4: Growth rate, or rate at which phase transformation takes place, is a function of interface temperature. For small degree of undercooling, this rate of growth can be approximated using a linear function of temperature [35].

In the model, the growth rate takes the form of interface response function. Such function relates the normal velocity of the interface, v_{int}, to the deviation of the interface

temperature, T_{int}, from the equilibrium melting point, T_{melt}. Our model uses the linear form of Eq. (2.17)

$$v_{int} = K|T_{int} - T_m| \tag{2.17}$$

where K is a proportionality constant. The value of this proportionality constant was determined by comparing simulated and experimental LGL values under various irradiation conditions. With this method, K was determined to be 7.0cm·s^{-1}·K^{-1}, whereas previous studies have placed the value of this constant in the range of 6.7-7.2cm·s^{-1}·K^{-1} [31, 32]. The linear form is valid for the degree of undercooling seen in liquid metal systems such as silicon [35]. Thus, starting with the energy barrier between solid and liquid phases, a simple relationship between solid-liquid interface velocity and undercooling was established. Although the kinetics of solidification at the solid-liquid interface are simple, the non-isothermal environment and the merging of interfaces which occur as solid phase regions grow and coalesce mean that interface position, as a function of time, will not have an analytical form. Instead of having a simple shape as shown in Fig. 2.5(a), in general, the interface will be an irregularly shaped surface that moves with time as shown in Fig. 2.5(b).

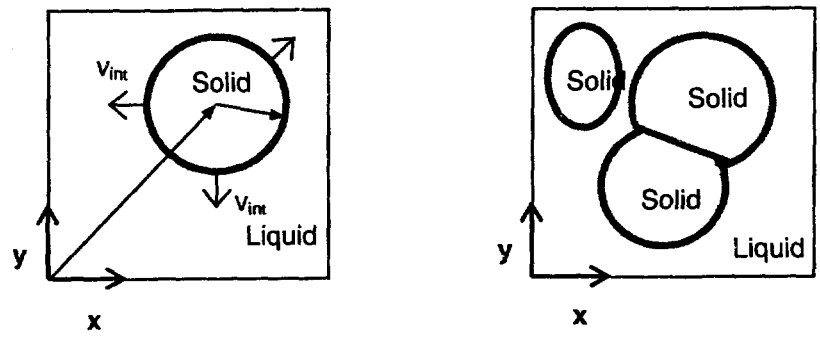

Figure 2.5 (a) and (b):

(a) Simplistic geometrical representation of the interface shape bounding a growing nucleus. (b) Practical situation depicting multiple growing and coalescing grains. In

that case, interface surfaces are not necessarily described by simple geometrical shapes.

In our model, this difficulty is partly addressed by a cellular automata (CA) algorithm that determines phase change without a priori knowledge of the shape of the interface. The algorithm works on a cell per cell basis to decide whether phase change will occur, based solely on the state of the cell and of its immediate neighbors. It also determines, from various possible scenarios, the way by which the interface migrates from a given cell to its neighbors. Another part of the difficulty is addressed by a set of functions that compute the displacement of the interface in the cell and the latent heat that is released or absorbed. To this end, the model defines 6 parameters that are needed to completely describe the state of a cell:

a) $\Phi(i, t)$: Phase of the i-th cell at time t. The possible values are 0 (solid), 1 (liquid) and ½ (containing interface).

b) $\Phi_n(i, t)$: Phase of the i-th cell's n-th neighbor at time t. $\Phi_n(i, t)$ can be obtained by simple translation operation, e.g., $\Phi_1(i, t) = \Phi(i+m, t)$ or $\Phi_{-1}(i, t) = \Phi(i-m, t)$, with m being determined by the cell numbering scheme specific to the geometry.

c) $F(i, t)$: Liquid fraction in the i-th cell at time t. The possible values range from 0 (completely solid) to 1 (completely liquid).

d) $T(i, t)$: Average temperature in the i-th cell at time t.

e) $x(i, t)$: Position of interface within the i-th cell at time t.

f) $dir(i, t)$: Orientation/type of interface in the i-th cell. There are 13 values representing 13 distinct orientations and interface types in 3-dimensional space.

The model then applies a set of rules to update the above parameters as the simulation progresses from one time step to the next. The rules allow the cell a certain level of "intelligence" to determine its future state. An example would be for a liquid cell with temperature above the melting point, in which case phase change does not occur. Another would be a cell that contains an interface within it, or in other words, is partly

solid and liquid. The interface will then move according to the interface response function (Eq. 2.17) and, depending on the original position and the direction of the interface, the interface may or may not migrate to adjacent cells. A key result is that, although the evolution in each cell is determined by local parameters, over time the configurations of the entire system resembles the propagation of contiguous surfaces seen in crystal growth.

2.3 Classical Nucleation Theory

Away from solid-liquid interfaces, transformation from liquid to solid starts with nucleation which forms of a solid phase critical nucleus and the solid-liquid interface that bounds it. In the liquid volume, transformation does not occur until such critical nucleus is spontaneously formed in a random manner by way of statistical fluctuation. The term critical implies that the size of the nucleus is such that its growth is energetically favorable and that it will survive and grow within the volume, until all volume is encompassed by it and others like it to complete transformation. Phase transformation is not the simple picture conveyed by the equilibrium formulation which assumes that temperature alone determines the phase of a material. Rather, the finite rate at which nucleation events occur results in the phenomenon of undercooling, where liquid phase persists even at temperatures well below melting point. Undercooling is explained as the result of an energy barrier to nucleation which, at the macroscopic level, results in a finite nucleation rate. In other words, temperature below melting point does not guarantee that nuclei will form everywhere in a volume. Instead, solid-liquid transformation will be a process limited by nucleation rate. Nucleation rate accounts for the different morphology as phase change is really a competition between nucleation and the growth of such nuclei. As an example, systems with higher quench rate will have higher nucleation rate which results in larger number but smaller size grains.

To simulate random nucleation, the model uses temperature and other data to evaluate the likelihood of nucleation in each element and in each time step. Once nucleation has occurred, the model then tracks its expanding boundary. As a nucleated solid grows, phase transformation will occur at its solid-liquid interface surface (as discussed in previous section). To evaluate the likelihood of nucleation the model uses the results of Classical Nucleation Theory (CNT).

Developed at the end of the 19th century, Classical Nucleation Theory establishes the relationship between the energy of formation of a nucleus to the rate of nucleation. It begins by considering the change in free energy that result when a spherical solid nucleus is formed:

$$\Delta G_r = \frac{4\pi}{3} r^3 \Delta G_{ls} + 4\pi r^2 \sigma \tag{2.18}$$

where r is the radius of the nucleus, ΔG_{ls} is the energy change per unit volume between the liquid and solid phase and σ is the surface energy of the sphere per unit area. As shown in fig. 2.6, the terms have opposite signs (the first is negative while the second is

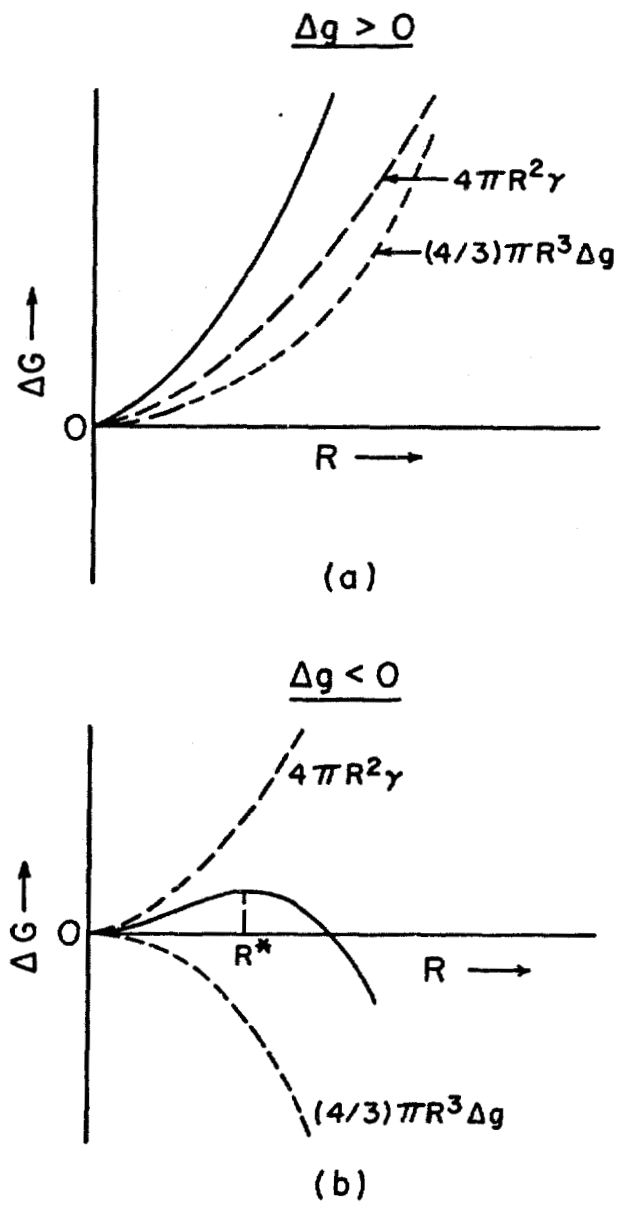

Fig.2.6: When surface energy is positive and free energy of formation is negative, an energy barrier is formed which correspond to a critical nucleus size beyond which spontaneous growth is favored [35].

positive) so there is r^* (critical) beyond which the change in free energy is negative. Thus the growth of a nucleus with $r > r^*$ will be favored while a nucleus with $r < r^*$ will shrink. r^* is obtained by setting the derivative of ΔG (with respect to r) to zero

$$r^* = -\frac{2\sigma}{\Delta G_{ls}} \tag{2.19}$$

Substituting (2.19) into (2.18), we can then solve for the value of the energy barrier

$$\Delta G^* = \frac{16\pi\sigma^3}{3\Delta G_{ls}{}^2} \tag{2.20}$$

This energy barrier enters into the exponent of the expression for the rate of nucleation (events/m^3.s)

$$I = I_{0V}(T) \cdot \exp\left\{-\frac{\Delta G_r^*}{3kT}\right\} \tag{2.21}$$

where I_{0V} is the kinetic prefactor, k is the Boltzmann's constant and T is the absolute temperature.

Substituting (2.20) into (2.21) we get the homogeneous nucleation rate

$$I_{\text{hom}} = I_{0V}(T) \cdot \exp\left\{-\frac{16 \cdot \pi \cdot \sigma^3(T)}{3kT \cdot \Delta G_{ls}}\right\} \tag{2.22}$$

We can obtain I as a function of the absolute temperature T by using the Turnbull approximation for ΔG_{ls}

$$\Delta G_{ls} = \Delta H_f \frac{(T_m - T)^2}{T} \tag{2.23}$$

where ΔH_f is the heat of formation and T_m is the equilibrium melting point. Furthermore, we can use a linearized form of surface energy

$$\sigma = 0.00035(T) \tag{2.24}$$

There are other models for $\Delta G_{ls}(T)$ and $\sigma(T)$ and these can be used in the subroutine as well.

So far we have outlined how homogeneous nucleation rate is derived as a function of temperature. Unlike homogeneous nucleation which occurs in the bulk of the liquid, heterogeneous nucleation occurs on catalytic surfaces in contact with the liquid. Homogeneous nucleation rate is always lower than heterogeneous nucleation rate since the barrier to nucleation is maximal for a spherical nucleus (in the case of heterogeneous nucleation) in the bulk. For a nuclei 'attached' to the catalytic surface, there is a factor $f(\theta)$ that reduces the energy barrier where θ is the contact angle - a measure of how well the nucleus adheres or 'wets' the catalytic surface. As shown in fig. 2.7.a, for $\theta = 180°$, the nucleus is a complete sphere. For $\theta < 180°$ shown in fig. 2.7.b, the nucleus is seen as a droplet that wets the catalytic surface. The heterogeneous rate includes the correction factor $f(\theta) = [2 - 3\cos(\theta) + \cos^3(\theta)]/4$ which accounts for the catalytic surface's role in lowering the energy barrier to nucleation as characterized by the contact angle θ. Defined for θ between 0° to 180°, $f(\theta)$ has minimum value of 0 at $\theta = 0°$ (activation energy is eliminated) and maximum value of 1 at $\theta = 180°$ (no effect) [35]. Typically, heterogeneous nucleation is the predominant mechanism because the catalytic surface reduces the energy barrier to nucleation, allowing it to occur at higher temperatures. In simulations using parameters in table 3.1, heterogeneous nucleation accounts for most (if not all) of the nucleation events since heat from the earliest heterogeneous events would quickly prevent the deeper undercooling required for homogeneous nucleation to occur.

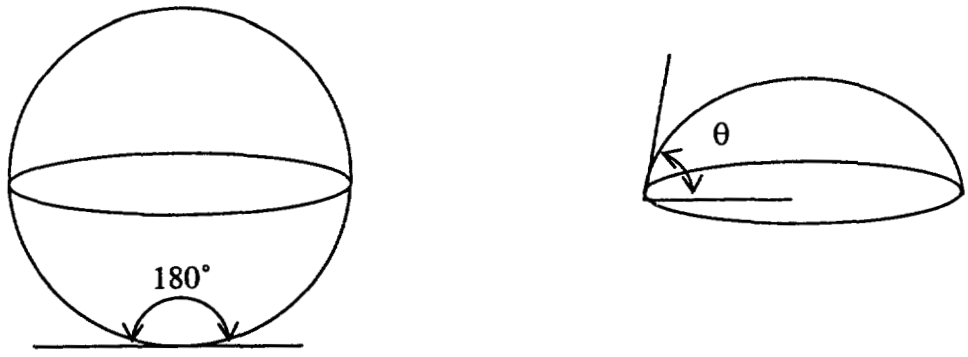

Fig. 2.7: (a) The volume of a nucleus with contact angle of 180° (a full sphere) is greater when compared to (b) a nucleus with contact angle of about 90°.

Substituting $f(\theta)$ into (2.21) we obtain the heterogeneous nucleation rate

$$I_{het} = I_{0a}(T) \cdot \exp\left\{-\frac{16 \cdot \pi \cdot \sigma^3(T) \cdot f(\theta)}{3kT \cdot \Delta G_{ls}}\right\} \tag{2.25}$$

In accordance with classical nucleation theory (CNT), the model accounts for nucleation that occurs in the bulk liquid (homogeneous) as well as on a catalytic surface such as the Si/glass interface (heterogeneous). In the model, homogeneous nucleation may occur in any fully liquid cell, resulting in the creation of a solid nucleus (hence a new solid-liquid interface) at the center of the cell. Heterogeneous nucleation, on the other hand, is

restricted to the liquid cells at the Si/glass interface to which a new nucleus would be attached. Nucleation is then followed by the isotropic growth of the solid nucleus in which the spherically shaped solid-liquid interface expands in all direction. Vertical growth, however, ends after the interface reaches the top or bottom surfaces of the silicon film and, henceforth, growth proceeds laterally along the plane of the film.

The expressions for homogeneous and heterogeneous nucleation rates established by CNT can then be used to calculate the likelihood of a cell remaining in liquid phase in each time step. This is done by using homogeneous Poisson statistics to calculate the probability of the absence of nucleation in the cell. This formulation treats a sequence of time steps as a series of homogeneous Poisson trials through which a critical solid nucleus may be formed. The duration of a time step, Δt, is typically 0.5ns. In the interval between t and $t + \Delta t$, the probability of the i-th cell remaining in liquid phase, $P_{i,t}^{LIQUID}$, is given by eq. 2.26.

$$P_{i,t}^{LIQUID} \equiv \exp\left[-\int_{t}^{t+\Delta t}\Gamma_i(\tau)\cdot d\tau\right] \equiv \exp\left[-\Gamma_{i,t}\cdot\Delta t\right] \tag{2.26}$$

where $\Gamma_i(\tau)$ is the instantaneous nucleation frequency of the cell which, at time t, is approximated by $\Gamma_{i,t}$, defined by the cell temperature which is assumed to be constant within the small time step Δt. For homogeneous nucleation occurring in the bulk fluid, $\Gamma_{i,t}$ is given by the product $[\Delta V \cdot I_v(T_{i,t})]$, where ΔV is the cell's volume and $I_v(T_{i,t})$ is the homogeneous nucleation rate (events/m^3·s) corresponding to the cell's temperature $T_{i,t}$ as given by eq. 2.22. For cells adjacent to catalytic surfaces (e.g., Si/glass interface), heterogeneous nucleation on the catalytic surface will be important and its frequency will be given by the product $[\Delta A \cdot I_a(T_{i,t})]$, where ΔA is area of the catalytic surface in contact with the cell and $I_a(T_{i,t})$ is the heterogeneous nucleation rate (events/m^2·s) as given by 2.25.

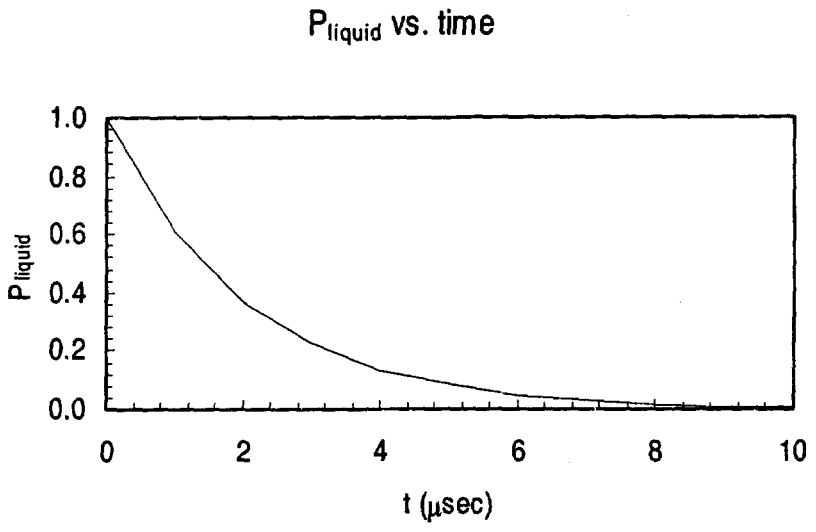

Fig 2.8: Probability of a cell remaining liquid decays with time

Simultaneously, the algorithm generates and assigns a random fraction to each cell at each time interval Δt for comparison with $P_{i,t}^{LIQUID}$. When the assigned number is larger than $P_{i,t}^{LIQUID}$, nucleation is said to occur within the cell. Since the probability (for a cell to remain liquid) decays as the temperature decreases, it will become more likely for nucleation to occur as quenching proceeds.

2.4 Random number generator

The previous section discussed how CNT is used to determine the likelihood of nucleation. The probability functions, by themselves, are not enough to simulate the random nature of the nucleation phenomena. In addition to probability functions, the model needs to generate a sequence of random fractions. At each time step, each element is assigned a random fraction to be compared to its probability of remaining in liquid

phase. To achieve this, at the beginning of the simulation the subroutine generates a sequence of unique integers. Each integer in the sequence is assigned to an element in the domain so that no two elements have the same integer. Each element then uses its unique integer as a seed to generate another random fraction as the simulation progress from one time step to the next. The sequence of fractions thus produced will be uniformly distributed between zero and one. The algorithm used to generate the sequence of random fractions is the Linear Congruential Method [40].

In the Linear Congruent Method, a sequence of seed integers $\langle X_n \rangle$ is obtained by the formula

$$X_{n+1} = (a \cdot X_n + c) \bmod m \tag{2.27}$$

where n is element number, m is modulus, a is multiplier and c is increment. The sequence of random fractions uniformly distributed between 0 and 1, $\langle U_t \rangle$ is obtained by the formula

$$X_{t+1} = (a \cdot X_t + c) \bmod m \tag{2.28}$$

$$U_t = \frac{X_t}{m_2} \tag{2.29}$$

where t is time step number.

Any congruential sequence repeats itself after a certain number, i.e., the sequence has a period which is determined by the particular choice of modulus, multiplier and increment. In our application, the period must be larger than the number of elements in the domain to be simulated in order for each element in the domain to have a unique seed. Number theory requires that for a sequence to have a period of m requires the following

a) c is relatively prime to m

b) $b = a - 1$ is a multiple of p, for every p dividing m

c) b is a multiple of 4 if m is a multiple of 4

For the sequence of integers for the seed, the following values were chosen

$c = 140003$

$a = 2821$

$m = 141000$, ($m \geq$ number of elements)

The prime factors of c are {191,733} while the prime factors of m are {2, 3, 5, 47} so c is relatively prime to m. Prime factor of b are {2, 3, 5, 47}. Lastly both m and b are divisible by 4. Thus the choices of a, c and m meet all the criteria listed above. For the sequence of fractions, the following values were chosen

$c = 623$

$a = 113601$

$m = 142000$

Since the prime factors of c, m and b are {7, 89}, {2, 5, 71} and {2, 5, 71} respectively. Lastly both m and b are again divisible by 4.

2.5 Summary

In conclusion, the hallmark of excimer laser crystallization process is its ability to melt thin silicon film without excessively heating the underlying substrate – the energy of the laser is absorbed within the silicon thin film. This is due to the strong absorption of UV light in silicon which is the result of band to band transition. The large grains that can arise from the subsequent transformation process result from the lateral growth of solid-phase crystal grain. The term lateral growth refers to the expansion of the crystal grain by inclusion of atoms from the liquid phase in a manner in which the crystal orientation is maintained. In the model, the rate of growth is represented by the interface velocity which is related to the interface undercooling via the interface response function. The region transformed through lateral growth is the focus of polysilicon technology which aims to produce material with maximum grain size. On the other hand, laser annealing in

the high energy region (i.e. sufficient to induce complete melting), may cause random nucleation due to the inevitable undercooling in the completely melted liquid. CNT formulation allows the prediction of the temperature at which this nucleation is triggered. The model accounts for nucleation that occurs in the bulk liquid (homogeneous) as well as on a catalytic surface such as the Si/glass interface (heterogeneous). In the model, homogeneous nucleation may occur in any fully liquid cell and would result in the creation of a solid nucleus (hence a new solid-liquid interface) at the center of the cell. Heterogeneous nucleation, on the other hand, is restricted to the liquid cells at the Si/glass interface to which a new nucleus would be attached. Having reviewed the theoretical basis for the model, the next chapter will discuss how these theories are implemented into an algorithm for simulating ELC re-crystallization and what information can be gained from such simulations.

CHAPTER 3: IMPLEMENTATION AND FEATURES OF THE MODEL

If all the terms of the heat equation (eq.1.2) are determined for all elements, FEM could iteratively solve for the temperature distribution throughout the domain. Designed to work in conjunction with FEM analysis tool, the function of our model is to compute the last two terms (energy sources) on the right hand side of the heat equation for all the elements in the domain. Fig. 3.1 shows how the model enables the FEM tool to simulate ELC process. The model is constrained to using only the variables solved by FIDAP 8.6., the FEM analysis tool chosen for this investigation. Based on these variables, the model then determines the values of the two volumetric energy sources based on various formulas and rules so FIDAP 8.6 could solve for the final temperature distribution in each time step. The process is then repeated in the succeeding time steps. Though implemented in FORTRAN and specifically tailored for compatibility with FIDAP 8.6, the algorithm can be implemented for use with other numerical analysis tools. This chapter begins by outlining how the model computes the two volumetric energy sources representing absorbed laser energy and latent heat. Also in this chapter are presented examples of the various surfaces used to represent solid-liquid interface surfaces that might be created inside an element to demonstrate the necessity for a rule based decision process. Finally, the implementation of the decision process in the form of a cellular automata algorithm will be presented and the capabilities of the model will be demonstrated.

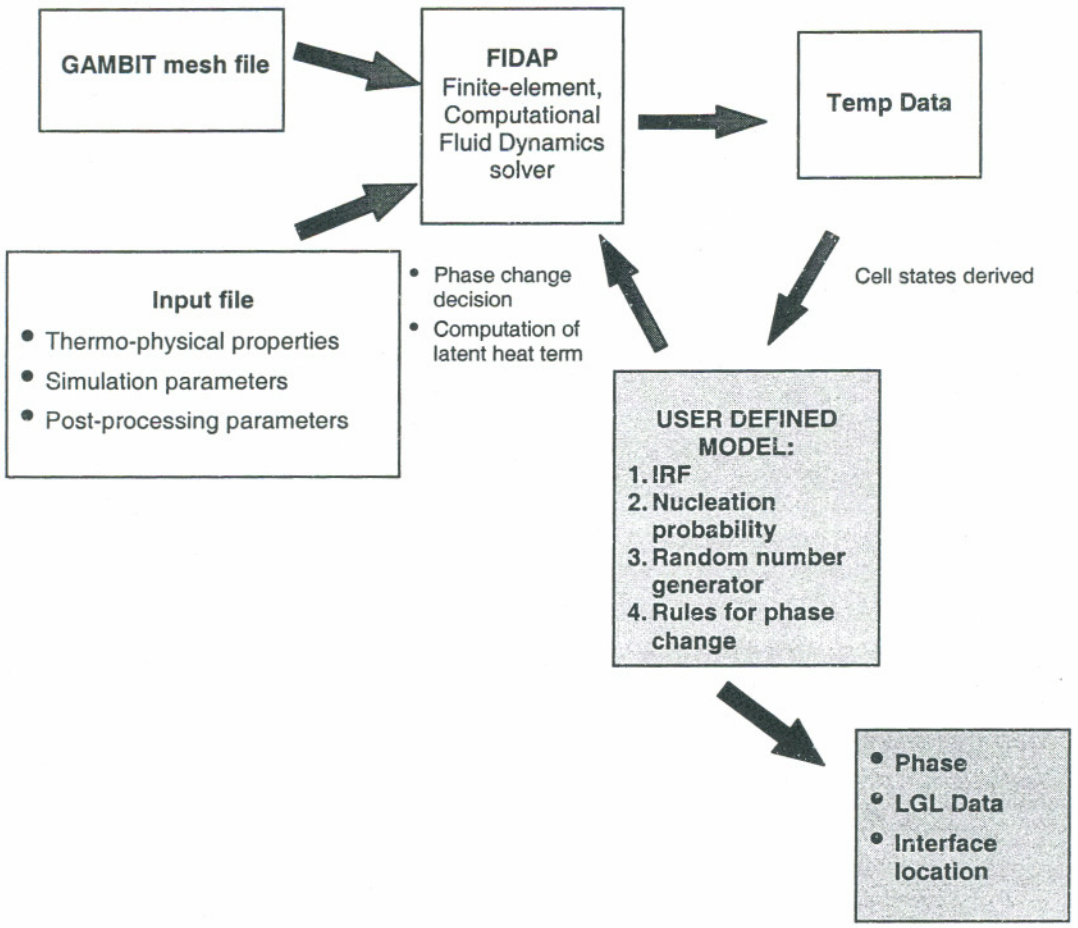

Fig. 3.1: Simulation of laser crystallization process by finite element method requires a user defined subroutine that incorporates the IRF, nucleation probability, random number generator and rules for phase change.

3.1 Laser energy source

Laser energy density or fluence (in mJ/cm^2), beam cross section (in cm^2) and laser profile (plotted in arbitrary units) are measurable experimental parameters. Therefore, it is useful to input these quantities directly into the model and have it compute the laser energy source (volumetric) representing the absorbed laser energy for each cell in the domain. To derive the relationship used in the model, we begin by considering the beam cross section and spatial profile as shown in fig.3.2.

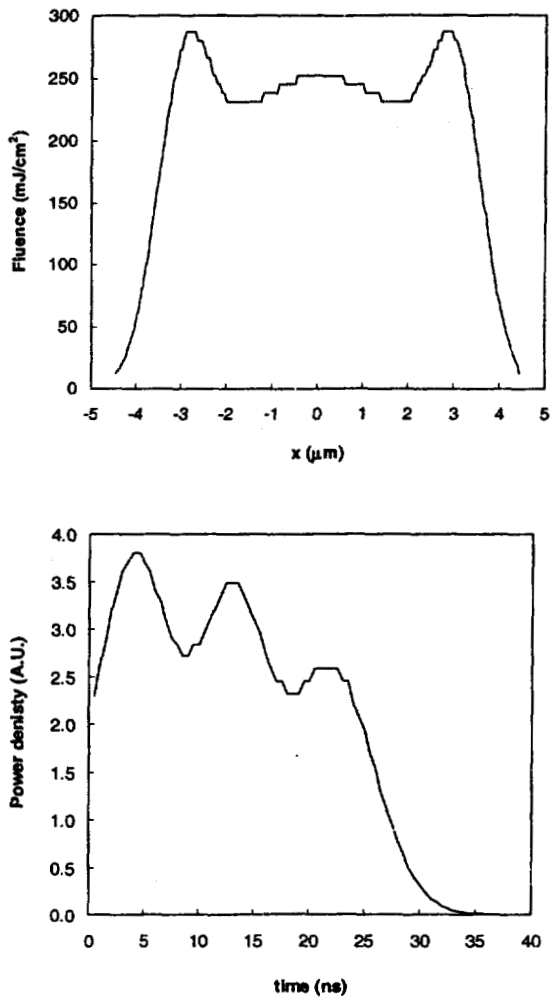

Fig.3.2: Laser profile, (a) spatial and (b) temporal

In typical experiments, the beam cross-section on the sample surface is 9μm wide by 10mm long. Along its width, W (along the x-direction), there's appreciable variation that constitutes the spatial profile whereas along its length, L (y-direction), the beam is assumed to be uniform. The profile can be represented by several Gaussian functions (unitless) varying in the x-directions such as

$$I_x(x) = \sum_i \alpha_{xi} \exp\left[-\frac{(\beta_{xi} - x)^2}{\gamma_{xi}}\right] \tag{3.1}$$

Similarly, the temporal profile can be described by the function (unitless)

$$I_t(t) = \sum_i \alpha_{ti} \exp\left[-\frac{(\beta_{ti} - t)^2}{\gamma_{ti}}\right] \tag{3.2}$$

where the sets of α's, β's and γ's must be determined based on the measured profile. Since the beam is uniform along the length L, the energy impinging on the film's surface per unit length (along L) is given by

$$E_L = \frac{ED \cdot A}{L} = \phi \int_0^W I_x(x)dx \int_0^\tau I_t(t)dt \tag{3.3}$$

where τ is the pulse duration, A is laser beam cross section, and ϕ is a proportionality constant (in mJ/cm^2·s) required for eq.3.3 to be true since $I_x(x)$ and $I_t(t)$ in general are not normalized.

$$\phi = \frac{ED \cdot A}{L}\left[\int_0^W I(x)dx \int_0^\tau I_t(t)dt\right]^{-1} \tag{3.4}$$

Using values for the absorption coefficient and reflectivity of silicon at λ = 308nm, laser energy term can be computed easily by applying Lambert's law for the energy distribution in an absorbing medium [35]. Thus, the power density, (in mJ/cm^2·s) in the film is given by

$$F(x,z) = (1-R)\cdot\phi\cdot I_x(x)\cdot I_t(t)\cdot e^{-2\alpha z} \tag{3.5}$$

where 2α is the absorption coefficient and R is the reflectivity of silicon. The energy absorbed by the segment of film between z and $z+\delta$

$$E_{z,z+\delta}(x) = F(x,z) - F(x,z+\delta) = (1-R)\cdot\phi\cdot I_x(x)\cdot I_t(t)\cdot\left[e^{-2\alpha z} - e^{-2\alpha(z+\delta)}\right] \tag{3.6}$$

The volumetric source in the segment of film is given by

$$\Delta S(x,z) = \frac{(1-R)\cdot\phi\cdot I_x(x)\cdot I_t(t)}{\delta\cdot\tau}\left[e^{-2\alpha z} - e^{-2\alpha(z+\delta)}\right] \tag{3.7}$$

which decreases as z (depth into the film) increases.

3.2 Latent heat source terms

With the exception of random nucleation, phase transformation occurs only at the solid-liquid interface. In the previous chapter, the interface response function (IRF) was introduced because it defines the relationship between the velocity of the interface (along its normal direction) and the interface temperature. In order to compute the latent energy involved in the transformation, the model uses the IRF to determine the precise amount of displacement along a particular direction as a function of the local temperature. Here we will discuss in more detail how the volumetric energy source representing the latent heat is derived.

It should be made clear that what is meant by interface temperature is simply the average of the nodal temperatures of an element containing an interface. Using the normal interface velocity defined by IRF, the displacement in the *i*-th element in the *t*-th time step with duration of τ is given by

$$\Delta r(i,t) = v_{int}\tau \tag{3.8}$$

As the interface surface in the *i*-th cell during *t*-th time step is displaced by $\Delta r(i,t)$, a fraction of the cell's volume, $\Delta F(i,t)$, undergoes phase transformation. The fraction of the cell that is transformed is commensurate to the displacement of the interface surface. The latent heat that is generated (or consumed) is given by

$$S_2(i,t) = \frac{H_{ls}\rho}{\Delta t} \cdot \Delta F(i,t) \tag{3.9}$$

where ρ is density, c_p is specific heat and ΔH_{ls} is the latent heat of solidification. To compute $\Delta F(i,t)$, however, requires additional decision making process as there are various formulas correlating $\Delta r(i,t)$ to $\Delta F(i,t)$ that the model can use depending on the type or orientation of interface surface in question.

$\Delta F(i,t)$ is determined not only by the displacement, $\Delta r(i,t)$, of the interface surface during the particular time step but also by the orientation (type) of the interface surface. The model defines various types of interface surfaces based on their orientations. Several of these surfaces are shown in fig. 3.3(a) through (c). The element is 50nm wide by 50nm long by 10nm tall. Taking the x-y plane to be parallel to the two largest sides of the cell, the interface orientation shown in 3.3(a) are parallel to the x or y axis. An interface surface with such orientation, (to be referred to as an x or y surface) moves along either the x or the y direction, as indicated by the arrow. For an x or y surfaces, the rules allow it to move to the adjacent cells in front of or behind it along the x or y direction. When an interface moves from one cell to the next, the surface orientation does not change. 3.3(b) shows a different type of surface, to be referred to as x-y surface, with its normal directed along the diagonal of the cell. When an x-y surface moves into neighboring cells, it generates new surfaces in 3 cells. Moving into the neighboring cell along the diagonal, the surface will maintain its x-y orientation. In addition to the diagonal direction, in the cells along the x and y directions, new surfaces will be created with orientations in the x and y direction, respectively. The last example is shown in Fig. 3.3(c) shows a surface

termed the z surface. Fig. 3.3(d) is unique in that the tetrahedral surface represents a spherical nucleus that is attached to the bottom of the cell. This cube at the bottom of the cell represents a solid phase nucleus formed by heterogeneous nucleation on a catalytic surface.

In order to track an interface surface and to precisely compute $\Delta F(i,t)$, a frame of reference is required. However, a single, global frame of reference will not be useful (nor easy to implement) in a cellular automata algorithm. For this reason, a more flexible way of providing spatial reference to each of the moving interfaces was devised. It involves, again, a set of algebraic formulas and rules to establish a frame of reference that can be used in computing a singular displacement that occurs within a time step. In a sense, this approach allows each interface to 'carry along' its own frame of reference for the purpose of computing its new position. As an example of the problem that must be resolved by the algorithm, consider again the interface shown in 3.3(b). As it advances, the algorithm must determine the phase transformation within the four cells through which the interface will sweep. The algorithm begins by determining the commensurate displacement based on the IRF and the type of interface surface in question. Based on its current location and the orientation, the algorithm then computes its new position. Because, in this case, three new surfaces are generated in the adjacent three cells, the algorithm needs to compute the source terms in four different cells.

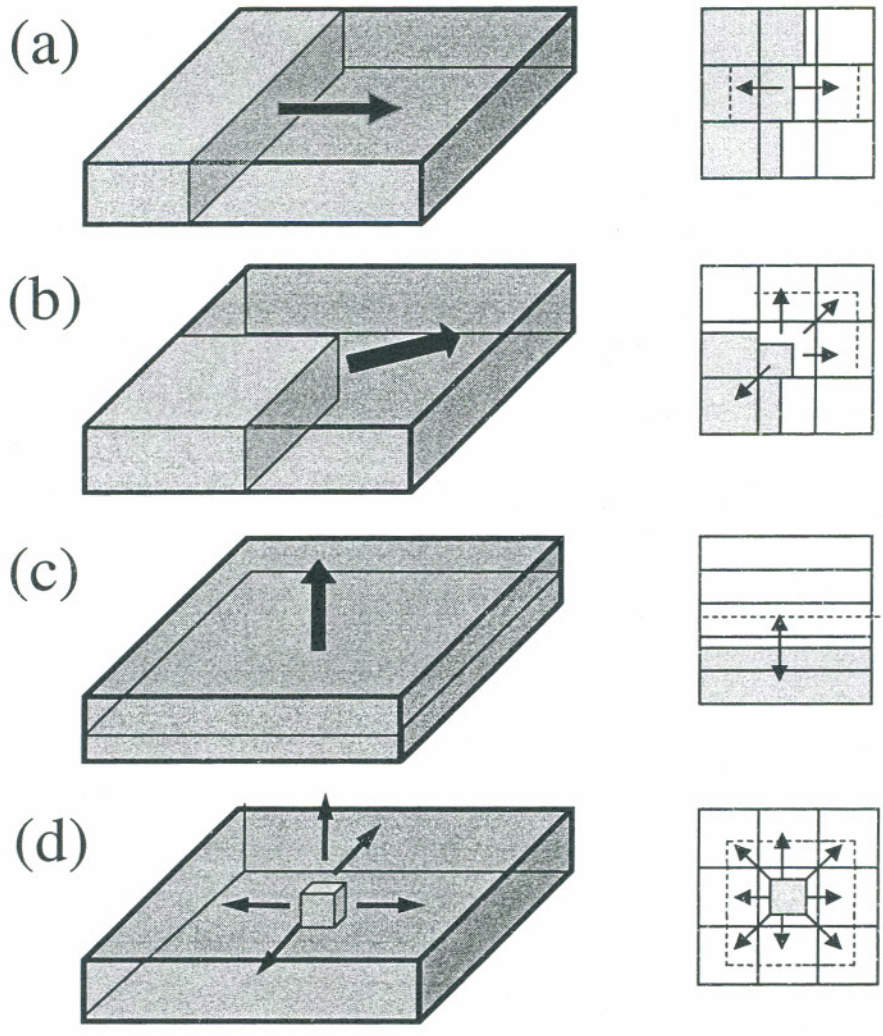

Fig. 3.3(a) through 3.3(c): Several examples of representations of the various forms that solid-liquid interfaces may take in a cell and the rules that define how they propagate into neighboring cells (new surfaces shown by dashed lines).

To provide a spatial reference, the variable $p(i,t)$ is employed to enable the measurement of the new interface position relative to the current interface position within the cell. The propagation of the various interfaces and the resulting transformation are defined by the following correlations:

$$p(i,t) = p(i,t-1) + \Delta x(i,t) \tag{3.10}$$

$$\Delta F(i,t) = \frac{\Delta x(i,t)}{L} \tag{3.11}$$

where L is the width of the cell and Δx is the displacement along the x direction. For an interface shown in fig. 3(b) the equations are

$$p(i,t) = p(i,t-1) + \Omega \cdot \Delta x(i,t) \tag{3.12}$$

$$\Delta F(i,t) = \frac{p(i,t)^2 - p(i,t-1)^2}{L^2} \tag{3.13}$$

where Ω is a predetermined correction factor. For interface shown in fig. 3(c) the equations are

$$p(i,t) = p(i,t-1) + \Delta z(i,t) \tag{3.14}$$

$$\Delta F_{Liquid}(i,t) = \frac{\Delta z(i,t)}{h} \tag{3.15}$$

where Δz is the displacement along the z (vertical) direction and h is the height of the cell. For interface shown in fig. 3.3(d) the equations are

$$p(i,t) = p(i,t-1) + \Omega \cdot \Delta l(i,t) \tag{3.16}$$

$$\Delta F(i,t) = \frac{p(i,t)^3 - p(i,t-1)^3}{h \cdot \left(\frac{L}{2}\right)^2} \tag{3.17}$$

It is clear from previous discussions that although predicting interface displacement by IRF is straightforward, the displacement may not necessarily be physically consistent. First, rules are needed to determine how the various surface types propagate across cell boundaries during a time step. Second, rules are needed to determine whether certain movement (as directed by the IRF) is physically consistent. The rules enable the algorithm to do the following:

1. Correlate interface displacement, $\Delta r(i,t)$, to the fraction volume converted, $\Delta F(i,t)$.
2. Determine how a single interface moves across the boundaries between two or more cells (interface jumps from one cell to other cells) to become multiple interfaces in multiple cells to mimic movements of curved surfaces.
3. Recognize when two interfaces meet as two solid grains coalesce and parts of their boundaries merge.

In this model, this rule-based decision process is accomplished by a cellular automata algorithm that is applied to all elements in a domain for each time step in the course of a simulation. Rule based decision process 'synchronize' the independent interfaces so that the resulting configuration represents contiguous solid-liquid interfaces.

3.3 Implementation the algorithm for use with FIDAP

The implementation of the algorithm enables the model to: (1) locate the initial position of all solid-liquid interfaces immediately after laser pulse ends by identifying elements that are partly liquid and solid and from this point onwards, (2) keep track of the movement of each of interfaces surfaces and calculate the resulting latent heat. The algorithm achieves these by taking in current information pertaining *only* to the element and its immediate neighbors and then applying various criteria and rules to arrive at a decision. In this manner, the algorithm controls the movement of individual interfaces so that, as a collective, these interfaces constitute larger, dynamic liquid-solid interfaces that bound all solid phase grains and lateral growth regions. For this reason, the algorithm includes rules that prevent, for instance, surface discontinuity and other situations that are not physically consistent while at the same time maintains the normal velocity at the interface as given by the IRF.

In every time step during the course of a simulation, the algorithm is called to its task of determining the energy sources in an element. In a single time step, the algorithm

repeats this task for each element in the domain. Once the energy sources have been determined in the entire domain, the FEM equations are solved iteratively. In a single time step there may be two iteration loops in the FEM procedure. The first iteration proceeds (with fixed duration of time step, e.g. 0.5ns) until the change in nodal temperature distribution become negligible or, in other words, temperature distribution has sufficiently converged. The final temperature distribution then becomes the solution of the FEM equations for that particular time step. The second iteration is a provision for when convergence fails to occur after a prescribed iteration cycle. In this case, duration of time step is decreased and the procedure is repeated. To increase computation speed, the values given by the model are stored for use in the first iteration. Re-calculation is done only when convergence fails to occur and time interval is changed so that the source energy values and/or decisions need adjusting.

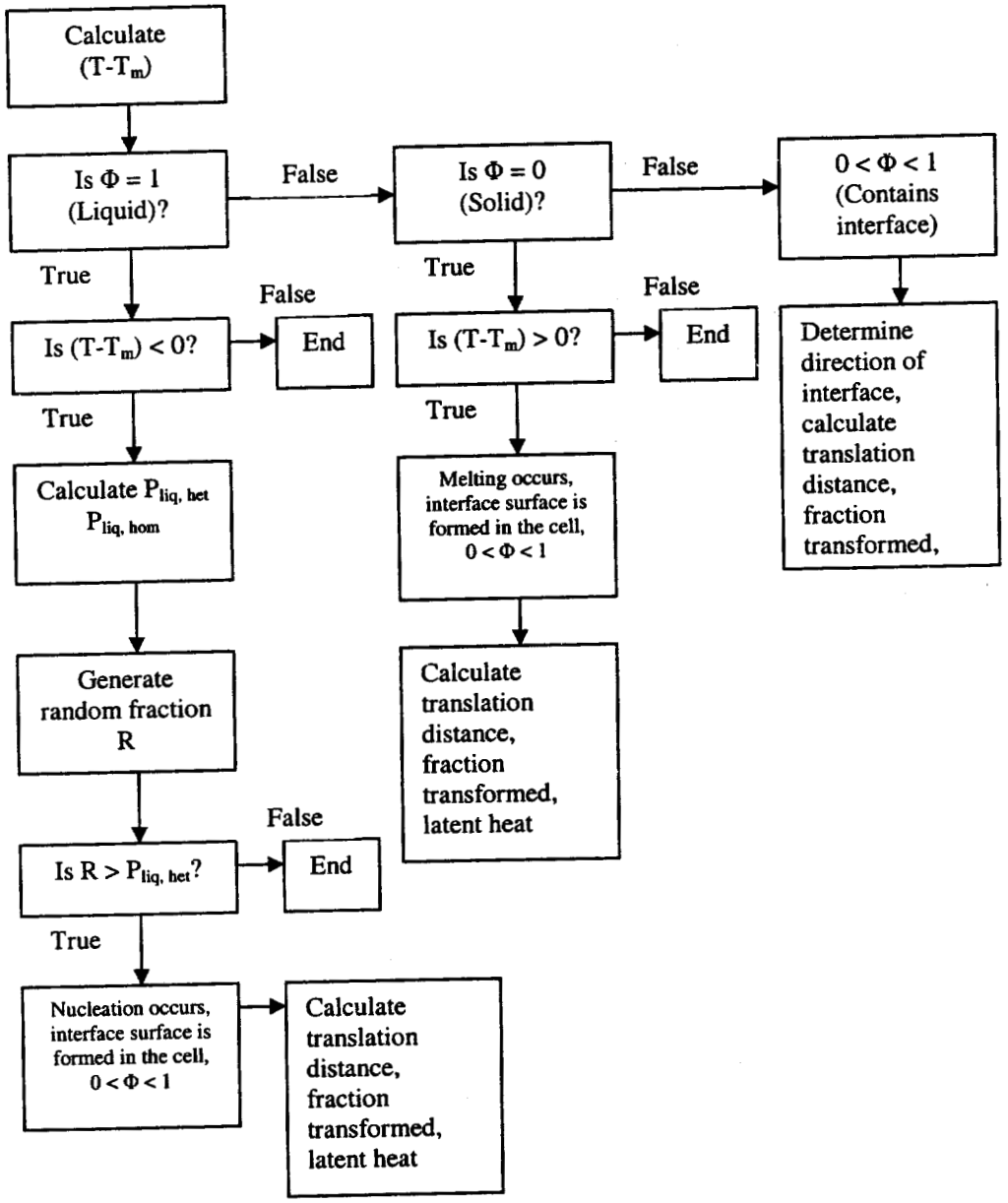

Fig. 3.4: Algorithm for random nucleation and the movement of solid-liquid interface.

Starting with the governing heat equation, it can be said that the model's purpose is to provide the FEM procedure with the volumetric energy sources that represent absorbed laser energy and phase transformation. Because phase transformation occurs at solid-liquid interface, the model has the capability to track its movement. In a liquid phase region, the model will be able to simulate random nucleation. Aside from computing absorbed laser energy, in each time step the model needs to determine the following about a particular element:

1. Whether or not the element contains an interface.
2. If the element contains an interface, which direction and by how much will the interface move and how this interface will be transmitted to neighboring elements?
3. If the element does not contain an interface, will nucleation occur or not?

The decisions are based on various parameters of the element which had been described in Chapter 2 and for convenience are again shown here:

g) $\Phi(i, t)$: Phase of the i-th cell at time t. The possible values are 0 (solid), 1 (liquid) and ½ (containing interface).

h) $\Phi_n(i, t)$: Phase of the i-th cell's n-th neighbor at time t. $\Phi_n(i, t)$ can be obtained by simple translation operation, e.g., $\Phi_1(i, t) = \Phi(i+m, t)$ or $\Phi_{-1}(i, t) = \Phi(i-m, t)$, with m being determined by the cell numbering scheme specific to the geometry.

i) $F(i, t)$: Liquid fraction in the i-th cell at time t. The possible values range from 0 (completely solid) to 1 (completely liquid).

j) $T(i, t)$: Average temperature in the i-th cell at time t.

k) $x(i, t)$: Position of interface within the i-th cell at time t.

l) $dir(i, t)$: Orientation/type of interface in the i-th cell. There are 13 values representing 13 distinct orientations and interface types in 3-dimensional space.

At time t, Latent heat term of the i-th cell is a function of :

a) Its phase at t-1, $\Phi(i,t)$

b) Phase of neighbor cells at t-1, $\Phi_n(i,t)$

c) Its temperature at t-1, $T(i,t)$

d) Position of interface within it, $x(i,t)$

The model then applies a set of rules to update the above parameters as the simulation progresses from one time step to the next. After it goes through the decision making process, the model than computes the source terms

$$S_H(i,t) = S_H(H(i,t-1), \Phi(i,t\text{-}1), T(i,t\text{-}1), x(i,t\text{-}1), T(i,t\text{-}1)) \tag{3.18}$$

It is noted here that implementation of the model for use with FIDAP requires it to follow the specific cell numbering scheme adopted by FIDAP for a particular domain [43]. In order to access information about neighboring cells the model must know how element numbers translate into cell position through the domain as FIDAP applies a distinct numbering scheme to each mesh created. Thus, if i identify the current element, the element numbers of the neighboring cells can be obtained by simple translation rules involving appropriate integers. For example, in a 2-dimensional mesh comprising of square elements, each element is surrounded by 8 neighbors as shown in fig 3.5.

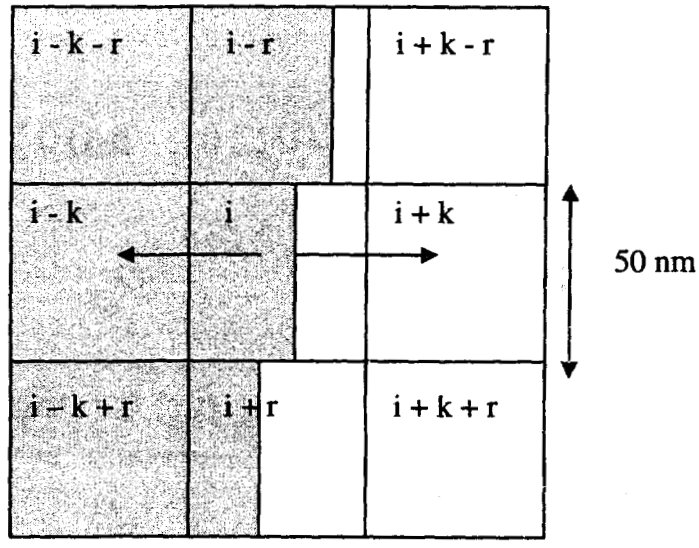

Fig 3.5: Element numbering system determines how to access information about nearest neighbors.

Since each side of an element is 50nm long, if the center of the *i*-th element is located at (x,y) the following relationships hold:

Neighbor	Cell number	Coordinate
1	i – k – r	(x-50, y-50)
2	I – r	(x, y-50)
3	i + k – r	(x+50, y-50)
4	i – k	(x-50, y)
5	i + k	(x+50, y)
6	i - k + r	(x-50, y+50)
7	i + r	(x, y+50)
8	i + k + r	(x+50, y+50)

3.4 Simulation features

Fig. 3.6 shows the simulated physical domain comprising of a 50nm thick silicon layer on a 3μm long x 20μm wide x 5μm thick glass substrate to match the materials use in actual process. The stack is irradiated by 9μm wide laser beam (λ = 308nm). The a-Si domain is divided into equal volumes, or cells, each with dimensions of 50nm long x 50nm wide x 10nm tall.

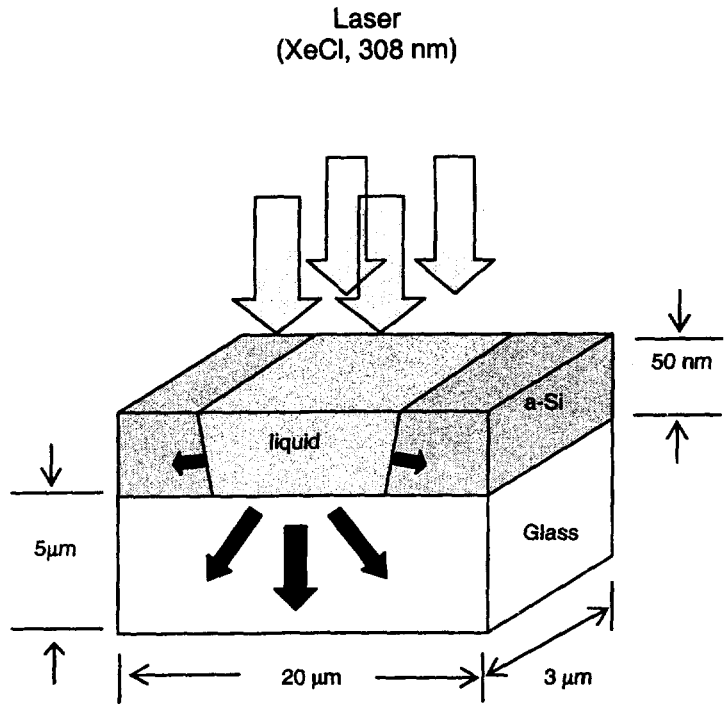

Figure 3.6: Illustration of the physical domain used in our simulations. A XeCl laser beam (308 nm) irradiates the substrate and melts the Si film deposited on the substrate. Heat diffuses away from molten region as indicated by solid arrows. The domain modeled is 3μm long x 20μm wide x 5μm tall. The typical a-Si film thickness is 50nm.

The simulation provides detailed information about the solidification process that occurs under non-equilibrium conditions of ELA. Fig. 3.7(a) shows the temperature history of a cell in the film, which is seen to rise to about 1500K as the film melts. It then rises even further for the remainder of the pulse duration, after which the film quenches. After about 50ns, the undercooling initiates random nucleation in the film with subsequent rise in temperature due to the released latent heat. This is in contrast to the equilibrium case (shown by the dashed line) that does not take into account undercooling and nucleation. Fig. 3.7(b) shows the distribution of temperatures at which nucleation events occur, demonstrating the random nature of nucleation. Fig. 3.8(a) is an example of

the simulation's graphical output: a snapshot of re-solidification process showing the expanding lateral growth areas and nucleated grains. From a similar image of a completely re-solidified domain, the LGL can be measured as the distance from the edge of the laterally crystallized region to the beginning of the nucleated region. Fig. 3.8(b) is the corresponding temperature field vividly showing the exact locations where phase change is occurring, i.e. at the moving solid-liquid interfaces at the edge of the laterally-crystallized region and at the perimeter of growing nuclei.

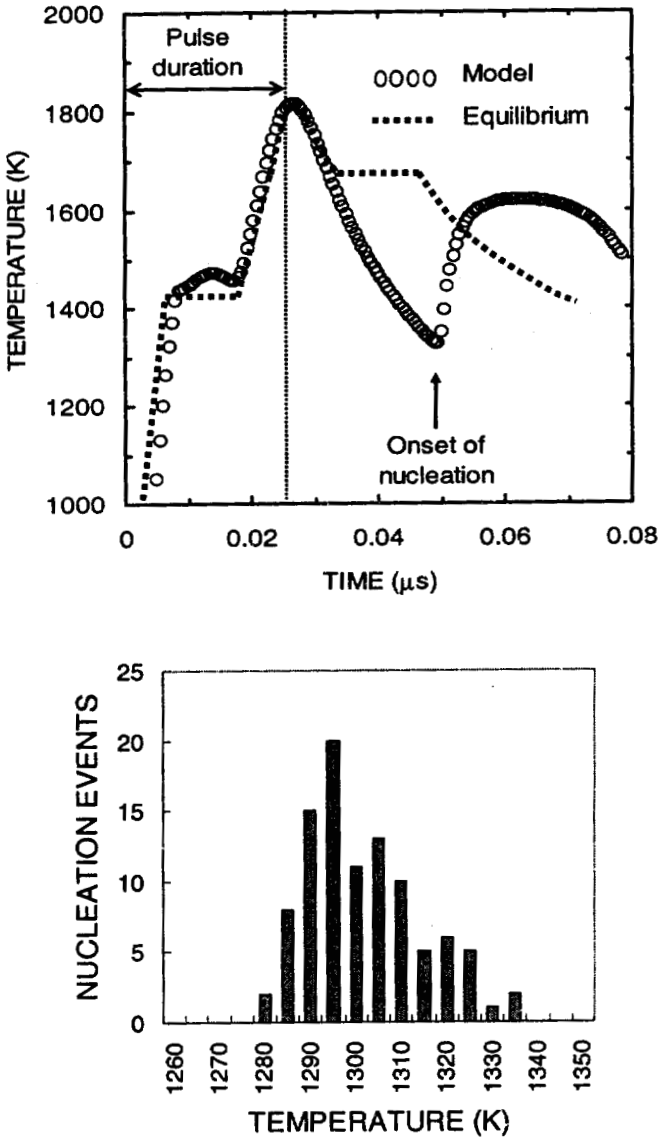

Figure 3.7: (a) Temperature history on the Si-glass interface at the beam center (50nm-thick film irradiated at RT and with 400mJ/cm^2). (b) Distribution of temperatures at which nucleation occur.

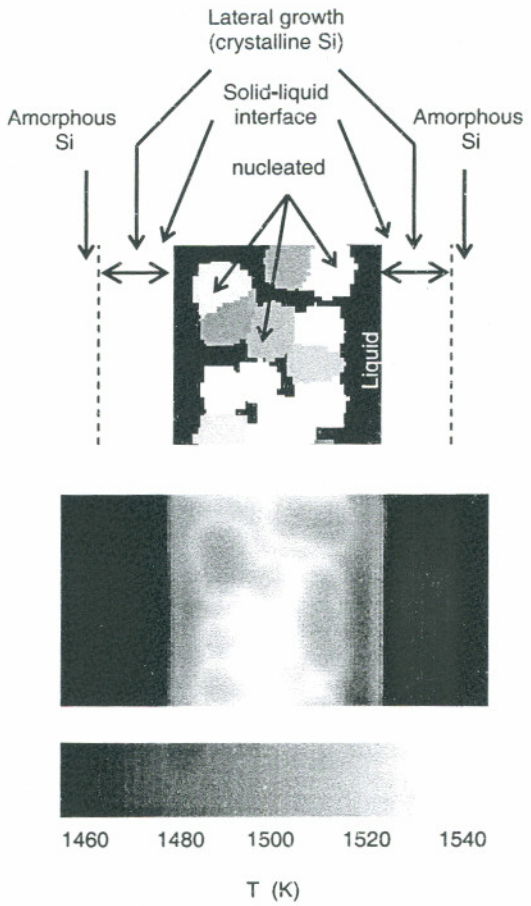

Figure 3.8: (a) Snapshot of the simulated poly-Si microstructure showing lateral growth and distinct grains arising from stochastic nucleation. (b) Bright areas in temperature field indicate localized release of latent heat at the solid-liquid interface and correspond to the boundaries of the growing grains.

3.5 Validating the model

In order to test the validity of the model, samples with 30nm, 50nm and 100nm-thick amorphous Si films on glass substrates were annealed by single 28ns pulses using 9μm x 10mm shaped-beamlets of XeCl laser (308nm). The corresponding LGL was measured by observing Secco-etched samples with a scanning electron microscope (SEM). The range of the laser fluence was chosen to completely melt the film. In the case of simulations, LGL was extracted by the method described in the previous section. Fig. 3.9 shows that the simulated LGL match well with LGL values measured from the annealed samples. This match was obtained using the set of thermo-physical parameters shown in Table 3.1 [8, 33, 41]. As the sensitivity analysis will show, closer match for 30nm and 100nm-thick films can be obtained if contact angle (θ), surface energy (σ), kinetic prefactor (I_a) or interface response function proportionality constant (K) were allowed to slightly vary as a function of the film thickness. Such process-specific set of parameters, however, is not convenient for screening simulations. Therefore, we have adopted the global parameter set of Table 3.1, accepting the slight error associated with this set in LGL predictions.

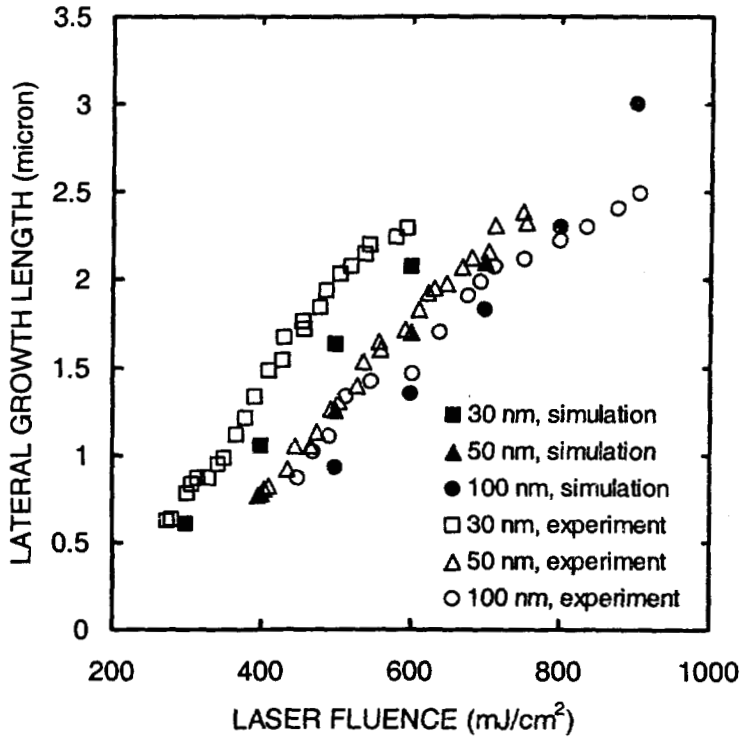

Figure 3.9: Simulated versus experimentally measured LGL as a function of the film thickness and the laser fluence. The model parameters used to match the experimental data were: $\theta = 70^{\circ}$ (contact angle), $\sigma = 0.40 J \cdot m^{-2}$ (surface energy), $I_a = 10^{27} m^{-2} \cdot s^{-1}$ (kinetic prefacer) and $K = 7.0 cm \cdot s^{-1} \cdot K^{-1}$ (IRF proportionality constant).

Table 3.1. Thermo-physical parameters used for the simulations [8, 33, 41].

Density, ρ	c-Si, a-Si, l-Si	2.33 $g \cdot cm^{-3}$
	Glass	2.54 $g \cdot cm^{-3}$
Enthalpy, H_m	c-Si	1799 $J \cdot g^{-1}$
	a-Si	1148 $J \cdot g^{-1}$
Equilibrium melting point, T_m	c-Si	1683 K
	a-Si	1420 K
Thermal conductivity, k	c-Si, a-Si, l-Si	k(T)
	Glass	1.2 $W \cdot m^{-1} \cdot K^{-1}$
Specific heat, c_p	c-Si, a-Si, l-Si	$C_p(T)$
	Glass	1.0 $J \cdot g^{-1} \cdot K^{-1}$
Reflectivity, R (AU)	a-Si	0.58
	l-Si	0.72
Absorptivity, α (at 308 nm)	a-Si	$2 \cdot 10^6$ cm^{-1}
	l-Si	$2 \cdot 10^6$ cm^{-1}
Kinetic prefactor (homogeneous nucleation), I_{ov}	l-Si	10^{39} $m^{-3} \cdot s^{-1}$
Kinetic prefactor (heterogeneous nucleation), I_{oa}	l-Si	10^{27} $m^{-2} \cdot s^{-1}$
Contact angle (heterogeneous nucleation), θ	l-Si	70°
Surface energy, σ	l-Si	0.40 $J \cdot m^{-2}$

3.6 Summary

In conclusion, an algorithm was developed to perform the following tasks: (1) determine when and where phase transformation occur through a set of rules based on local variables, (2) compute the resulting latent heat (3) simulate transformation via stochastic nucleation based CNT expressions. The algorithm enables proper simulation of grain growth and random nucleation. The simulation yield important information on the transformation, such as interface velocity, quenching rate and LGL which are important attributes for evaluating the process. The next chapter will discuss how the model was validated and its response to select key parameters.

CHAPTER 4: ANALYSIS AND DISCUSSION

In the previous chapter, it was shown that the model can effectively predict the extent of lateral solidification (LGL) for a range of laser fluence and film thickness. In this chapter, the sensitivity of LGL to various model parameters is analyzed. This demonstrates the behavior of the model which is useful for qualitative understanding of the mechanisms of nucleation and growth as well as for fine tuning of model parameters. Simulations were also done to study the effect of laser fluence and substrate temperature on key attributes such as quench rate and interface velocity. The rest of the chapter discusses applications of the model to test new ELC processes. This illustrates how simulations can help to verify the efficacy of new ELC concepts before actual experiments are set up.

4.1 Sensitivity study

To better understand the transformation of a region of completely melted silicon on a glass substrate, a set of simulations were done to study the effect of select model parameters. Table 4.1 presents a sensitivity analysis of key simulation responses such as LGL and nucleation count (which correlates to average grain size) for 50nm film and fluence of 500mJ/cm^2. Four model parameters were allowed to vary and the responses were recorded in Table 4.1. The model parameters of interest are: (1) contact angle (θ), (2) surface energy (σ), (3) interface response function (IRF) proportionality constant (K), and (4) kinetic prefactor for heterogeneous nucleation (I_{oa}). These parameters were varied

using a factor-at-a-time scheme, i.e. vary one factor and leave the rest at their nominal settings.

Table 4.1. Sensitivity analysis of key simulation responses to variations in model parameters θ, σ, I_a and K.

θ (°)	σ ($J \cdot m^{-2}$)	I_a ($m^{-2} \cdot s^{-1}$)	K ($cm \cdot s^{-1} \cdot K^{-1}$)	LGL (μm)	Nucleation temperature (average) (K)	Quenching time (average) (μs)	Nucleation count (μm^{-2})
N	N	N	N	1.175	1301	0.041	4.8
65	N	N	N	0.85	1343	0.036	6.6
75	N	N	N	1.35	1261	0.046	3.0
N	**0.35**	N	N	0.65	1370	0.032	7.5
N	**0.45**	N	N	2.025	1233	0.051	2.9
N	N	$\mathbf{10^{24}}$	N	1.825	1188	0.059	1.4
N	N	$\mathbf{10^{30}}$	N	0.625	1370	0.031	9.8
N	N	N	**3.5**	0.4	1289	0.039	11.3
N	N	N	**10.5**	1.45	1309	0.041	2.6

N = nominal setting (θ = 70°, σ = 0.40 $J \cdot m^{-2}$, $I_a = 10^{27}$ $m^{-2} \cdot s^{-1}$, K = 7 $cm \cdot s^{1} \cdot K^{-1}$)

The data in Table 4.1 suggest that, in the simulation, the extent of lateral growth is mainly determined by the duration of time needed for the film to quench from its maximum temperature, T_{MAX}, to a lower temperature (average), T_{NUC}, which will induce nucleation. Within this duration of time, referred to as quenching time, t_Q, the melt front is allowed to advance before it is eventually stopped by the proliferation of randomly generated nuclei. The model parameters θ, σ and I_{oa} directly determine the nucleation

probability and T_{NUC}, but do not directly affect the quench rate. Since it takes longer time to quench to lower temperatures, lower T_{NUC} allows the melt front to travel over a longer distance and results in longer LGL. Table 4.1 shows LGL increasing with θ, as deeper undercooling (or, equivalently, larger t_Q) is required for nucleation. This is expected as larger θ relates to larger energy barrier to heterogeneous nucleation. Similarly, LGL increases with σ. This is expected because higher surface energy, σ, relates to higher energy barriers to both homogeneous and heterogeneous nucleation. Also, LGL decreases with increasing kinetic prefactor (I_{oa}) values. Larger I_{oa} results in higher nucleation frequency, which translates to higher T_{NUC} (requiring lesser degree of undercooling to induce nucleation). Thus, when θ, σ and I_{oa} are varied, LGL increases when T_{NUC} decreases. This point is confirmed by the observed trend in LGL versus T_{NUC} shown in Fig. 4.1(a) and LGL versus t_Q in Fig. 4.1(b) for data corresponding to each combination of θ, σ and I_{oa} used in the sensitivity analysis. On the other hand, Fig. 4.1(c) shows how varying the IRF proportionality constant (K) affects LGL and nucleation count, despite of the relatively little impact it has on t_Q or T_{NUC} (see Table 4.1). In this case, K determines the interface velocity (thus, directly affecting LGL), which in turn affects the average temperature surrounding a nucleation site as well as the rate at which liquid volume is consumed by grain growth (thus, affecting nucleation count). Furthermore, despite the strong impact that nucleation parameters (I_{oa}, θ, and σ) have on T_{NUC} and LGL, their impact on the nucleation count is much weaker (see Table 4.1). As an example, compared to the orders of magnitude variation in I_{oa}, the total nucleation events changes only slightly (see Table 4.1). This demonstrates that nucleation, as described by the model, is a self-limiting process. As film temperature approaches T_{NUC}, a number of nuclei appear and the latent heat released quickly diminishes the probability of further nucleation.

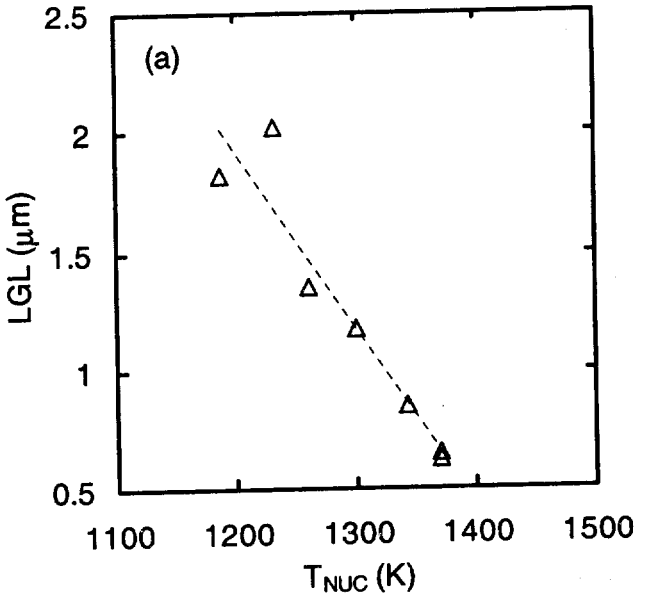
(a)
LGL (μm)
2.5
2
1.5
1
0.5
1100
1200
1300
1400
1500
T_{NUC} (K)

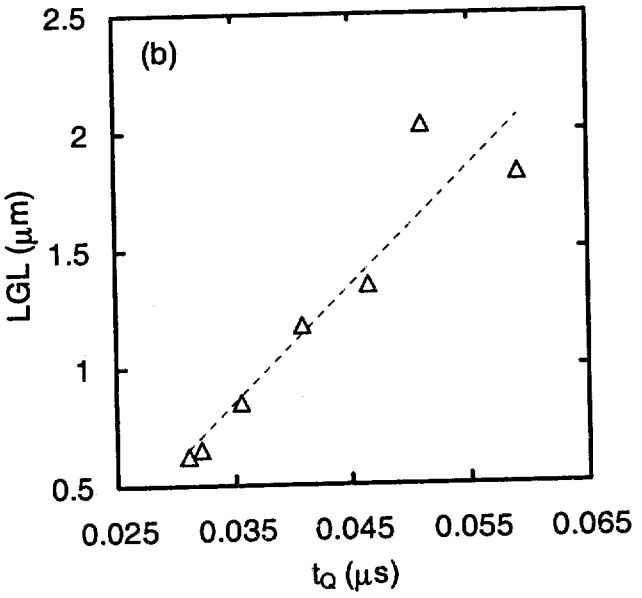
(b)
LGL (μm)
2.5
2
1.5
1
0.5
0.025
0.035
0.045
0.055
0.065
t_Q (μs)

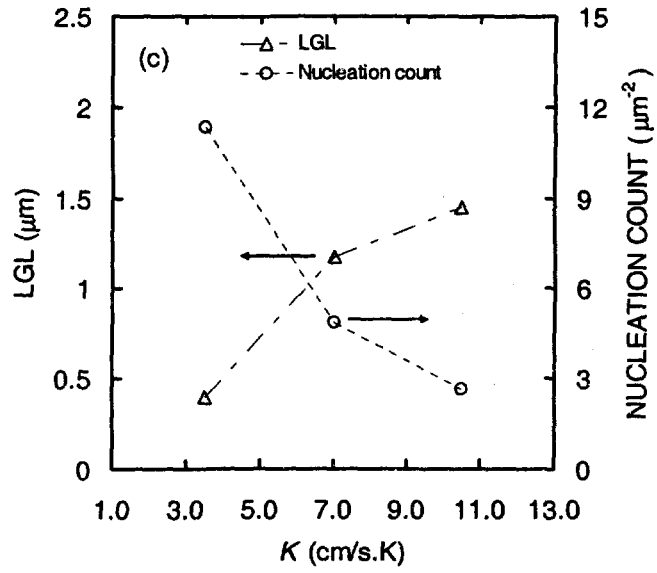

Figure 4.1: (a),(b) Plots of LGL vs. nucleation temperature (T_{NUC}), and quenching time (t_Q), respectively, corresponding to combinations of θ (contact angle), σ (surface energy) and I_a (heterogeneous nucleation kinetic prefactor) used in the sensitivity study of Table 4.1. (c) Although IRF proportionality constant, K, does not strongly impact nucleation temperature (see Table 4.1), it strongly affects interface velocity and ultimately LGL and nucleation count.

While Fig. 3.9 shows our best effort to match simulated and experimental LGL, the parameters determined from such comparison have not yield similar microstructure as characterized by nucleation count/μm^2. Fig. 4.2(a) shows the experimental microstructure of a 100nm film annealed at 486mJ/cm^2 and Fig. 4.2(b) shows the corresponding simulation result on the same scale. The experimental microstructure shows nucleation count of ~300counts/μm^2, while the simulations yield ~15counts/μm^2. For similar irradiation conditions, simulation typically yields average grain size of 10 to 20 times

larger than what is measured experimentally. Since LGL is largely determined by t_Q, the match in LGL values suggests that simulated T_{NUC} and t_Q are close to actual values. At the same time, the disagreement in the final nucleation count suggests that, at T_{NUC}, the model underestimates the nucleation rate, perhaps by neglecting additional phase transformation mechanisms. One such mechanism is athermal nucleation, which possibly could play a significant role in the highly transient conditions of ELA [41, 42]. A closer match of nucleation count (while maintaining a close match of LGL) is possible if we allow two different IRF proportionality constants, one controlling the interface of laterally grown domains and the other controlling the interfaces of nucleated domains. Fig. 4.2(c) shows a nucleation frequency of ~70counts/μm^2 for the simulated domain, when K (nucleated domains) is assumed to be 1.4 $cm \cdot s^{-1} \cdot K^{-1}$, while all other parameters are kept at their nominal settings. Of course, whether or not having two different K values in the model is physically consistent will have to be addressed by further investigation. It should be noted that the ELC process still far from the near-equilibrium conditions of Zone Melt Refining or Czochralski processes which are characterized by very low quenching rate of ~1/1000 °C/min. Therefore, ELC process will generate more defects within the crystalline material.

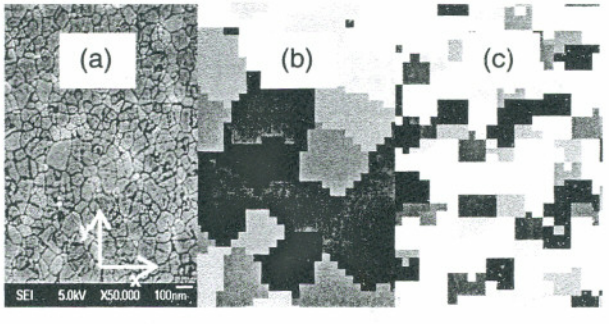

Figure 4.2: (a) SEM micrograph (planar view) of 100nm-thick film annealed at RT and 486mJ/cm^2 with ~300counts/μm^2. (b) Using nominal values for simulation parameters, the corresponding simulated microstructure (same scale) shows ~15counts/μm^2. (c) When the same case was simulated using K = 1.4$cm \cdot s^{-1} \cdot K^{-1}$ for the

***interface of nucleated domains*, a better match in nucleation density (~70counts/μm^2) was obtained.**

4.2 Effects of laser fluence and substrate temperature

Table 4.2 shows the effect of laser fluence on key simulation responses that describe the phase transformation occurring in the irradiated film. While T_{MAX} increases with laser fluence, lateral interface velocity is shown to decrease. This is due to the lesser degree of undercooling of the liquid silicon that is afforded by the higher melt temperature. Increased laser fluence is also found to increase t_Q. This allows the interface to travel over a longer distance and, despite of the decreasing lateral interface velocity, results in longer LGL. Based on this result, it is conceivable that LGL can be increased using advanced pulse shaping techniques that aim at reducing the quenching rate of the film, defined as $(T_{MAX}-T_{NUC})/t_Q$. Beyond increasing LGL, reducing the quenching rate of the film (i.e. decreasing the lateral growth velocity) can be beneficial for the structural quality of the laterally-grown region. Rapid lateral growth is more susceptible to structural defects that degrade the material quality. An upper limit to the interface velocity has been reported (25m/s), beyond which lateral growth is replaced by amorphization [43]. As the lateral interface velocity comes closer to this limit we expect higher rates of defect generation within the lateral-growth domain. Thus, the combination of long LGL with low quenching rate is highly desirable to maintain high structural quality.

One rather simple technique to reduce quenching rate is via substrate heating which has two effects of (1) lowering the laser energy required to reach melting temperature and, hence, (b) reducing the temperature gradient and rate of heat diffusion. Therefore, we have conducted further simulations to investigate the effects of substrate temperature. Table 4.3 shows the results of such simulations for 50nm-thick films

irradiated with a laser fluence of 400mJ/cm^2. The substrate is either at room temperature, 600K or 800K. These simulations show that heating the substrate further extends the t_Q and thus the longer LGL. We note that increasing substrate temperature results in the reduction of lateral interface velocity in a manner analogous to that observed when laser fluence is varied. However, heating the substrate is a more advantageous strategy, as the same LGL can be achieved with lower laser fluence (i.e. lower maximum film temperature). Once the film temperature exceeds the evaporation point of Si (~3000K), local evaporation of the film will commence. This is clearly an undesirable situation. Thus, independent control of the T_{MAX} and quenching rate is the best strategy for operating close to such extreme limits. As we will discuss in a forthcoming publication, beyond substrate heating, temporal pulse separation, as well as spatial beam splitting are equivalent approaches for exercising such independent control.

Table 4.2. Effects of laser fluence on simulation responses associated with the phase transformation of a 50nm-thick Si film (at RT).

Laser fluence ($mJ \cdot cm^{-2}$)	Maximum film temperature (K)	Lateral interface velocity ($m \cdot s^{-1}$)	Quenching time (average) (μs)	LGL (μm)
400	1682	17.6	0.021	0.80
500	2054	16.8	0.044	1.25
600	2418	14.5	0.061	1.70
700	2780	12.6	0.089	2.10

Table 4.3. Effect of substrate temperature on simulation responses associated with the phase transformation of a 50nm-thick Si film (at 400mJ/cm^2).

Substrate Temperature (K)	Maximum film temperature (K)	Lateral interface velocity (m·s^{-1})	Quenching time (average) (μs)	LGL (μm)
298	1682	17.6	0.021	0.80
600	1942	15.2	0.052	1.52
800	2105	13.5	0.110	2.45

4.3. Simulation of multiple pulse irradiation schemes

An important feature of the ELC process is that LGL is largely determined by the length of time during which the solid-liquid interface can travel before T_{NUC} is reached and nucleation is triggered. Thus, to maximize LGL, the onset of nucleation must be delayed by controlling the quenching rate of the melt, which lead to the idea for multiple laser pulse irradiation. As an example, irradiation can be done using two pulses separated by a time delay. In this scenario, the film is melted by the first pulse which is then followed by the second pulse after a prescribed delay, to maintain sufficiently high melt temperature where nucleation is avoided. Another approach is to use multiple pulses with different pulse durations. To illustrate the value of ELC simulation in testing these ELC concepts, the results are presented below.

4.3.1. Two pulses with time delay

In this approach, the first pulse melts film, followed by a time delay in which film quenches. Then the second pulse is applied to raise film temperature to avoid nucleation. The start of the second pulse is determined by the onset of nucleation (predicted by simulation) – if it occurs later than the onset of nucleation, the technique will not be effective. The energy in the second pulse is only a fraction of the first pulse, sufficient only to raise the temperature to prevent nucleation while not exceeding the melting temperature of crystalline silicon.

Fig. 4.3 compares simulated temperature histories of single pulse versus two pulses separated by time delay and Table 4.4 compares the LGL produced. The second pulse's energy is 10%, 20% and 40% of the first pulse's energy. There is significant increase in LGL by using two pulses because the increase in temperature from the second pulse prevents nucleation from occurring while still maintaining supercooling required for lateral growth. LGL, however, saturates with increasing energy of the second pulse since higher temperature could mean interface boundary stops moving or even retreat. The implementation of this concept requires a pulse extender module. The beam would be split and one portion would be sent along a longer optical path. The time delay would typically range from one to few multiples of the pulse duration, ~30ns.

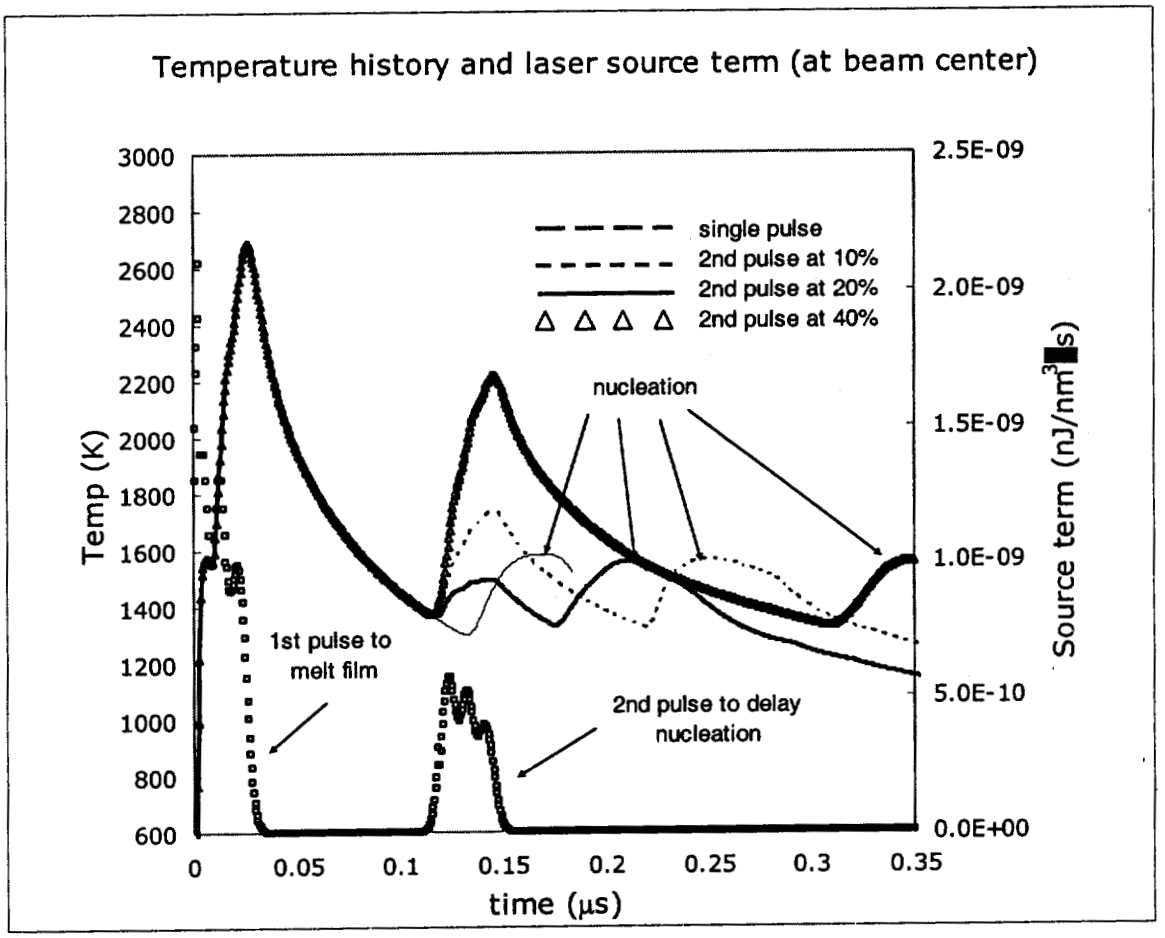

FIG. 4.3 Two pulses with time delay. The second pulse is applied to raise film temperature to prevent nucleation.

Table 4.4. 2nd pulse energy versus LGL.

Energy of 2nd pulse (%)	LGL (μm)
0	1.975
10	2.725
20	2.9
40	3.05

4.3.2 Triple pulse without delay

The triple pulse scheme has the same purpose: to control quenching by maintaining film temperature at a level where nucleation does not occur while maintaining lateral growth. The triple pulse scheme uses three pulses of different durations and energy density. The combinations are dictated by hardware considerations such as maximum energy density that can be absorbed by the beam shaping mask. Such a constraint arises when 1:1 projection system is used and the mask is exposed to same fluence as what is required to melt the film on the wafer. Otherwise, by using a 5:1 projection system, for example, fluence going through the mask is only 1/25 of what goes to the wafer surface. Triple pulse scheme uses a 28 ns pulse that goes through the beam shaping mask combined with a 28 ns and a 180 ns pulse that goes directly to the wafer. Energy densities of the 1st, 2nd and 3rd pulses are E_1, E_2 and E_3 respectively. Fig. 4.4 compares temperature histories of single pulse versus triple pulse scheme while Table 4.5 compares the LGL produced.

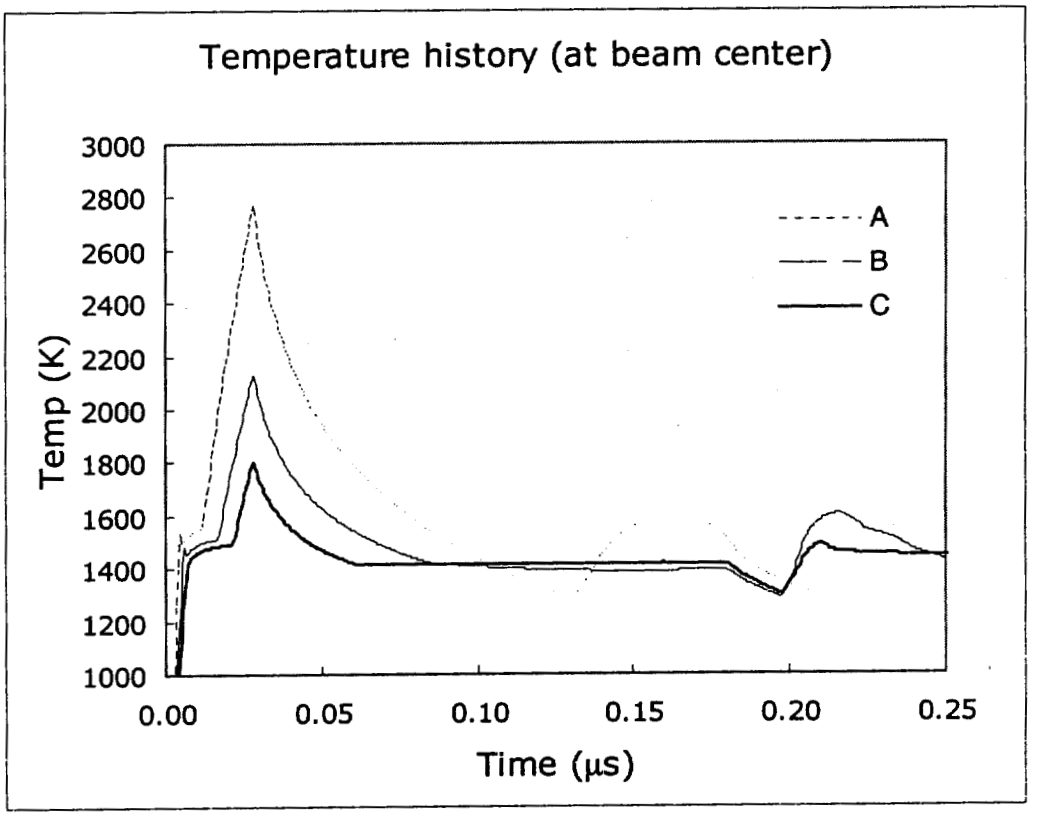

FIG. 4.4 The effects of triple pulse scheme. A is single pulse with $E_1 = 700$ mJ/cm^2, $E_2 = E_3 = 0$ mJ/cm^2. B uses $E_1 = 76$ mJ/cm^2, $E_2 = 312$ mJ/cm^2 and $E_3 = 305$ mJ/cm^2. C uses $E_1 = 97$ mJ/cm^2, $E_2 = 208$ mJ/cm^2 and $E_3 = 389$ mJ/ cm^2. Note that C results in lower film temperature.

Table 4.5. Triple pulse energy combination versus LGL.

Combination	LGL (μm)
A	1.975
B	2.725
C	2.9

The results of the simulations show that it is possible, with the triple pulse scheme, to lower the film temperature and increase LGL at the same time. Compared to the double pulse with time delay, this scheme also is advantageous since film temperature is significantly lower. The particular combinations of E_1, E_2 and E_3 were chosen so the triple pulse scheme is effective. The requirements for the triple pulse are:

1. Between t = 0 and t = 28 ns of irradiation, the combined energy of three pulses is sufficient to melt the film.
2. E_1 is below the limit for the mask.
3. Between t = 28 ns and t = 180 ns, the combined power of E_2 and E_3 will not cause film temperature to rise above melting temperature (so supercooling is maintained).

The combinations of energy densities of the three pulses fulfilling the above requirements determine the process window for the three pulse method.

CHAPTER 5: CONCLUSIONS

In any laser crystallization process, the goal is to produce films composed of large crystals. This is achieved by creating an environment which prefers transformation by way of lateral growth, with LGL as the measurable attribute. Lateral growth is transformation through the growth of existing grains rather than transformation through the creation of solid nuclei. Thus, LGL is directly proportional to quenching time. The development of a model comprising of (1) rules for phase change, (2) functions to compute the resulting latent heat and (3) a model for stochastic nucleation have resulted in a powerful simulation tool for predicting LGL. Simulations using the model have added to the understanding of non-equilibrium melting and solidification. Prediction of lateral growth can also be used to judge an annealing scenario based on its efficacy in creating an environment in which lateral growth is to be the dominant transformation mechanism. In practice, this is useful for predicting a process window, determining the pitch to use in sequential lateral solidification or studying the temperature profile within an irradiation field to anticipate thermal stress.

The model is especially useful for laser-crystallization process where many parameters and their interactions need to be optimized. Using the simulation tool, we can easily screen any conceived irradiation scheme for its efficacy and save experimental time and cost. Moreover, this simulation allows us to assess schemes that may require additional hardware than what is currently available in the laboratory. In that sense, simulation can effectively guide equipment selection/design. As an example, the triple pulse scheme shows comparable LGL of around 3μm though melting was achieved in considerably lower film temperature of ~1800 K, compared to ~2700 K for the normal process.

It has been mentioned that LGL is only one aspect of the crystallization process. Although LGL is direct measure of the extent of laterally grown material, it does not have information on the quality or structure within the laterally grown material. In a rapid quenching environment of laser crystallization, defects within the laterally grown grain would be inevitable. Also, the issues of mechanical stress that arises from the volume expansion of solid silicon which is released when sub-grain boundaries are formed and mass transfer that causes ridges to form where grain boundaries meet have not been addressed. Finite element analysis is well suited for the inclusion of such mechanical effects. Further experiments and development of the model could be done to relate the quenching characteristics (available currently) with various defect generation mechanisms and mechanical stress. Although the development of the current model has been based on the work of Im and co-workers, the adaptation of the transformation model to a standard finite modeling tool opens the door for future work to include film stress computation as one way of assessing defect generation within the laterally-grown region of the irradiated domain. Another avenue of development is the estimation of film stress and surface roughness induced by re-crystallization.

The simulation can also be extended to applications using different types of lasers with different absorption characteristics. For 308Å laser the absorption depth is shallow so relatively small amount energy is required to achieve melting without causing heat build up within the irradiated region. For this reason, simulation need only to focus on the a single shot, without considering the effects that previous shots have on temperature profile. This is because in ELC typical repetition rate is low enough so that the duration between shots is sufficient for the temperature to return to initial level. The use of other laser radiation that is absorbed by the glass substrates, for instance, may result in cumulative heating which, in multiple irradiation schemes, will certainly produce more complex temperature profile. In such a case, variables such as repetition rate or the amount of overlap of successive irradiations are likely to affect the steady state temperature profile. Here simulation can be critical in delineating the complex interaction

between these variables. In this way, simulation can then guide experimental works which otherwise, because of the various variables involved, will have to be extensive.

REFERENCES

1. S D. Brotherton, D. J. McCulloch, J. B. Clegg and J. P. Gowers, "Excimer-Laser-Annealed Poly-Si Thin-Film Transistors", *IEEE Trans. Elec. Dev.*, Vol. 40, No. 2, p. 407, 1993.

2. J. Levinson, F. R. Shepherd, P. J. Scanlon, W. D. Westwood, G. Este and M. Rider, "Conductivity behavior in polycrystalline semiconductor thin film transistors", *J. Appl. Phys.*, Vol. 53, No. 2, p. 1193, 1982.

3. A. Marmorstein, A. T. Voutsas and R. Solanki, "A systematic study of parameters affecting grain size and surface roughness in excimer laser annealed polysilicon thin films", *J. Appl. Phys.*, Vol. 82, No. 9, p. 4303, 1997.

4. R. S. Sposili and J. S. Im, "Line-scan sequential lateral solidification of Si thin films", *Appl. Phys. A*, Vol. 67, p. 273, 1998.

5. J. S. Im, M. A. Crowder, R. S. Sposili, J. P. Leonard, H. J. Kim, J. H. Yoon, V. V. Gupta, H. J. Song, and H. S. Cho, "Controlled Super-Lateral Growth of Si Films for Microstructural Manipulation and Optimization", *Phys. Stat. Sol. (a)*, Vol. 166, p. 603, 1998.

6. M. Lee, S. Moon, M. Hatano, K. Suzuki, and C. P. Grigoropoulos, "Relationship between fluence gradient and lateral grain growth in spatially controlled excimer laser crystallization of amorphous silicon films", *J. Appl. Phys.*, Vol. 88, No. 9, p. 4994, 2000.

7. M. Miyasaka and J. Stoemenos, "Excimer laser annealing of amorphous and solid-phase-crystallized silicon films", *J. Appl. Phys.*, Vol. 86, No. 10, p. 5556, 1999.

8. H. Kuriyama, S. Kiyama, S. Noguchi, T. Kuwahara, S. Ishida, T. Nohda, K. Sano, H. Iwata, H. Kawata, M. Osumi, S. Tsuda, S. Nakano and Y. Kuwano, "Enlargement of Poly-Si Film Grain Size by Excimer Laser Annealing and Its Application to High-Performance Poly-Si Thin Film Transistor", *Jpn. J. Appl. Phys.*, Vol. 30, p. 3700, 1991.

9. R. F. Wood and G. A. Geist, "Modeling of nonequilibrium melting and solidification in laser-irradiated materials", *Phys. Rev. B*, Vol. 34, No. 4, p. 2606, 1986.

10. J. Viatella, S. Lee, and R. Singh, "Selective Area Excimer-Laser Crystallization of Amorphous Silicon Thin Films", *J. Electrochem. Soc.*, Vol. 146, No. 12, p. 4605, 1999.

11. P. Baeri, S. U. Campisano, G. Foti, and E. Rimini, "A melting model for pulsing-laser annealing of implanted semiconductors", *J. Appl. Phys.*, Vol. 50, No. 2, p. 788, 1979.

12. E. Lueder, *Liquid Crystal Display,* Wiley-SID, Chichester, New York, 2001.

13. C. T. Angelis, C. A. Dimitriadis, M. Miyasaka, F. V. Farmakis, G. Kamarinos, J. Brini and J. Stoemenos, "Effect of excimer laser annealing on the structural and electrical properties of polycrystalline silicon thin-film transistors", *J. Appl. Phys.*, Vol. 86, No. 8, p. 4600, 1999.

14. A. T. Voutsas, "A new era of crystallization: advances in polysilicon crystallization and crystal engineering", *Applied Surface Science*, Vol. 208-209, p. 250, 2003.

15. Y. Z. Wang and O. O. Awadelkarim, "Metal-induced solid-phase crystallization of hydrogenated amorphous silicon: dependence on metal type and annealing temperature", *Appl. Phys. A*, Vol. 70, p. 587, 2000.

16. J. Poate and J. Mayer, *Laser Annealing of Semiconductors,* Academic Press, 2000.

17. J. S. Im, H. J. Kim and M. O. Thompson, "Phase transformation mechanisms involved in excimer laser crystallization of amorphous silicon films", *Appl. Phys. Lett.*, Vol. 63, No. 14, p. 1969, 1993.

18. J. S. Im and H. J. Kim, "On the super lateral growth phenomenon observed in excimer laser-induced crystallization of Si films", *Appl. Phys. Lett.*, Vol. 64, No. 17, p. 2303, 1994.

19. K. F. Kelton, "Crystal Nucleation in Liquids and Glasses", *Solid State Physics*, Vol 45, No. 75, 1991.

20. R. S. Sposili and J. S. Im, "Sequential lateral solidification of thin silicon films on SiO_2", *Appl. Phys. Lett.*, Vol. 69, No. 19, p. 2864, 1996.

21. H. J. Song and J. S. Im, "Single-crystal Si islands on SiO_2 obtained via excimer-laser irradiation of a patterned Si film", *Appl. Phys. Lett.*, Vol. 68, No. 22, p. 3165, 1996.

22. H. J. Kim and J. S. Im, "New excimer-laser-crystallization method for producing large-grained and grain boundary-location-controlled Si films for thin film transistors", *Appl. Phys. Lett.*, Vol. 68, No. 11, p. 1513, 1996.

23. R. S. Sposili, J. S. Im and M. A. Crowder, "Single-crystal Si films for thin-film transistor devices", *Appl. Phys. Lett.*, Vol. 70, No. 25, p. 3434, 1997.

24. M. A. Crowder, A. B. Limanov, J. S. Im, "Sub-grain Boundary Spacing in Directionally Crystallized Si Films Obtained via Sequential Lateral Solidification", *Mat. Res. Soc. Symp. Proc.*, Vol. 621, p. Q9.6.1, 2000.

25. J. P. Leonard, *Nucleation Rate Measurement in the Si-SiO_2 Thin Film System*, PhD Thesis, Columbia University, 2000.

26. G. Devaud and D. Turnbull, "Undercooling of molten silicon", *Appl. Phys. Lett.*, Vol. 4, No. 9, p. 844, 1985.

27. S. R. Stiffler, M. O. Thompson and P. S. Peercy, "Transient nucleation following pulsed-laser melting of thin silicon films", *Phys. Rev. B*, Vol. 43, No. 12, p. 9851, 1991.

28. Y. Shao and F. Spaepen, "Undercooling of bulk liquid silicon in an oxide flux", *J. Appl. Phys.*, Vol. 79, No. 6, p. 2981, 1996.

29. H. Song and J. Im, "Excimer-laser crystallization of patterned Si film at high themperatures via artificially controlled super-lateral growth", *Mat. Res. Soc. Symp. Proc.* Vol. 397, 459, 1996.

30. P. Baeri and S. Campisano, *Laser Annealing of Semiconductors*, edited by J. Poate and J. Mayer, Academic Press, New York, 1982.

31. V. V. Gupta, H. J. Song and J. S. Im, "Numerical analysis of excimer-laser-induced melting and solidification of thin Si films", *Appl. Phys. Lett.*, Vol. 71, No. 1, p. 99, 1997.

32. J. Leonard and J. Im, "Stochastic modeling of solid nucleation in supercooled liquids", *Appl. Phys. Lett.*, Vol. 78, No. 22, p. 3454, 2001.

33. J. Leonard, D. Kim, A. Limanov and J. Im, "3D Numerical Modeling of Laser Crystallization Processes in Silicon Thin Films", *Mater. Res. Soc. Symp. Proc.*, Vol. 580, p.233, 2000.

34. R. W. Ditchburn, *Light*, Dover, New York, 1991, Ch. 15.

35. A. K. Jena and M. C. Chaturvedi, *Phase Transformation in Materials*, Prentice Hall, New Jersey, 1992.

36. E.I. Givargizov, *Oriented Crystallization on Amorphous Substrates*, Plenum Press, New York, 1991, Ch. 1.

37. J.W. Christian, *The Theory of Transformations in Metals and Alloys: Part 1 Equilibrium and General Kinetic Theory*, Pergamon Press, Oxford, 1975, Ch. 10.

38. D.T. Wu, "Nucleation Theory", *Solid State Physics*, Vol. 50, p. 37, 1997.

39. S. Stoyanov, "Nucleation Theory For High and Low Supersaturations", *Current Topics in Material Science*, Vol. 3, edited by E. Kaldis, North Holland Publishing Co., Amsterdam, 1979.

40. D. E. Knuth, *The Art of Computer Programming Vol. 2: Seminumerical Algorithms*, Addison-Wesley, Reading, Massachusets, 1998.

41. J. Im, V. Gupta and M. Crowder, "On determining the relevance of athermal nucleation in rapidly quenched liquids", *Appl. Phys. Lett.*, Vol. 72, No. 6, p. 662, 1998.

42. J. Im, V. Gupta and M. Crowder (unpublished).

43. P. Bucksbaum and J. Bokor, "Rapid Melting and Regrowth Velocities in Silicon Heated by Ultraviolet Picosecond Laser Pulses", *Phys. Rev. Lett.*, Vol. 53 No. 2, p. 182, 1984.

44. *FIDAP 8 Theory Manual*, Fluent Inc., Lebanon, New Hampshire, 1996.

45. R. Kern, G. Le Lay, J.J. Metois, "Basic Mechanisms In Early Stages Of Epitaxy", *Current Topics in Material Science*, Vol. 3, North Holland Publishing Co., Amsterdam, 1979.

46. R.T. DeHoff, *Thermodynamics in Materials Science*, Mc Graw Hill, New York, 1993.

47. M. Ohring, *The Materials Science of Thin Films*, Academic Press, Boston, 1992.

48. D.M. Etter, *Structured FORTRAN 77 For Engineers and Scientists*, Benjamin Cummings Publishing, Redwood City, 1990.

49. G.B. Davis, T.R. Hoffman, *FORTRAN 77: A Structured Disciplined Style*, Mc Graw Hill, 1988.

50. A. J. Chapman, *Fundamentals of Heat Transfer*, Collier Macmillan, New York, 1987.

51. S. Wolfram, *The Mathematica Book*, Cambridge University Press, Cambridge, 1996.

52. D. H. Norrie and G. deVries, *Introduction to Finite Element Analysis*, Academic Press, New York, 1978.

53. P. Hartman, *Crystal Growth: An Introduction*, American Elsevier, New York, 1973, Ch. 2.

54. W. H. Press, *Numerical Recipes in C*, Cambridge University Press, Cambridge, 1997.

55. W. Tiller, *The Science of Crystallization: macroscopic phenomena and defect generation*, Cambridge University Press, Cambridge, 1992.

56. K. Huebner, E. Thornton, T. Byrom, *The Finite Element Method for Engineers*, John Wiley and Sons, New York, 1995.

57. D.J Ehrlich and J.Y. Tsao, *Laser Microfabrication: Thin Film Processes and Lithography*, Academic Press, San Diego, 1989, Ch. 4.

58. D. N. Kouvatsos, A. T. Voutsas, M. K. Hatalis, "High-Performance Thin-Film Transistors in Large Grain Size Deposited by Thermal Decomposition of Disilane", *IEEE Trans. Elec. Dev.*, Vol. 43, No. 9, p. 1399, 1996.

59. R. Wood and G. Giles, "Macroscopic theory of pulsed, laser annealing. I. Thermal transport and melting", *Phys. Rev. B*, Vol. 23, No.6, p. 2923, 1981.

60. S. Wolf, *Silicon Processing for the VLSI Era,* Lattice Press, Sunset Beach, 1995.

Vita

Hidayat Kisdarjono was born in Bandung, Indonesia on June 4th, 1970. In 1988 he entered Institut Teknologi Bandung. After graduating from the Department of Physics in the summer of 1993, he worked at the Inter-University Center for Microelectronics in Bandung.

Hidayat entered Oregon Graduate Institute in 1994 and graduated with an M.S. from the Electrical Engineering and Applied Physics Department in the spring of 1995. He then went on to work for Applied Materials in Singapore until the fall of 1999.

Hidayat returned to Oregon Graduate Institute in the fall of 1999 to pursue a Ph.D. He was involved in a project sponsored by Intel Component Research Laboratories to characterize optical properties of dielectric films. His Ph.D. research was sponsored by Sharp Laboratories of America.

During the course of his time at OGI, Hidayat contributed the following publications:

1. H. Kisdarjono, T. Voutsas, R. Solanki, "Three-dimensional simulation of rapid melting and re-solidification of thin Si films by excimer laser annealing", *J. Appl. Phys.*, Vol. 94, p. 4374, 2003.

2. H. Kisdarjono, T. Voutsas, R. Solanki, "Modeling laser beam temporal separation effects for projection laser crystallization", *Proc. SPIE*, Vol. 5004. p. 2003.

3. T. Voutsas, H. Kisdarjono, R. Solanki, A. Kumar, "Numerical simulation of non-equilibrium, ultra-rapid heating of Si-thin films by nanosecond-pulse excimer laser", *Proc. SISPAD 2001*, p. 132, Springer-Verlag, Wien, 2001.

4. H. Kisdarjono, T. Voutsas, R. Solanki, A. Kumar, "Simulation of transient temperature profiles during ELA and relation to process parameters", *Proc. SPIE*, Vol. 4295, p. 41, 2001.